Miner Deposita
DOI 10.1007/s00126-012-0444-1

ARTICLE

Age and tectonomagmatic setting of the Eocene Çöpler–Kabataş magmatic complex and porphyry-epithermal Au deposit, East Central Anatolia, Turkey

Ali İmer · Jeremy P. Richards · Robert A. Creaser

Received: 5 March 2012 / Accepted: 25 September 2012

Abstract The Çöpler epithermal Au deposit and related subeconomic porphyry Cu–Au deposit is hosted by the middle Eocene Çöpler–Kabataş magmatic complex in central eastern Anatolia. The intrusive rocks of the complex were emplaced into Late Paleozoic–Mesozoic metamorphosed sedimentary basement rocks near the northeastern margin of the Tauride-Anatolide Block. Igneous biotite from two samples of the magmatic complex yielded $^{40}Ar/^{39}Ar$ plateau ages of 43.75±0.26 Ma and 44.19±0.23, whereas igneous hornblende from a third sample yielded a plateau age of 44.13±0.38. These ages closely overlap with $^{40}Ar/^{39}Ar$ ages of hydrothermal sericite (44.44±0.28 Ma) and biotite (43.84±0.26 Ma), and Re–Os ages from two molybdenite samples (44.6±0.2 and 43.9±0.2 Ma) suggesting a short-lived (<1 my) magmatic and hydrothermal history at Çöpler. No suitable minerals were found that could be used to date the epithermal system, but it is inferred to be close in age to the precursor porphyry system. The Çöpler–Kabataş intrusive rocks show I-type calc-alkaline affinities. Their normalized trace element patterns show enrichments in large ion lithophile and light rare earth elements and relative depletions in middle and heavy rare earth elements, resembling magmas generated in convergent margins. However, given its distance from the coeval Eocene Maden–Helete volcanic arc, the complex is interpreted to be formed in a back-arc setting, in response to Paleocene slab roll-back and upper-plate extension. The tectonomagmatic environment of porphyry-epithermal mineralization at Çöpler is comparable to some other isolated back-arc porphyry systems such as Bajo de la Alumbrera (Argentina) or Bingham Canyon (USA).

Keywords Porphyry Cu–Au · Epithermal Au · Tauride-Anatolide Block · Central eastern Anatolia · Turkey · Middle Eocene

Editorial handling: T. Bissig

Electronic supplementary material The online version of this article (doi:10.1007/s00126-012-0444-1) contains supplementary material, which is available to authorized users.

A. İmer · J. P. Richards (✉) · R. A. Creaser
Department of Earth and Atmospheric Sciences,
University of Alberta,
Edmonton, AB, Canada T6G 2E3
e-mail: Jeremy.Richards@ualberta.ca

A. İmer
e-mail: Imer@ualberta.ca

R. A. Creaser
e-mail: Robert.Creaser@ualberta.ca

Introduction

Convergent and collisional orogens worldwide are host to a wide range of magmatic rocks and associated mineral deposit types (e.g., Janković 1977; Solomon 1990; Hedenquist and Lowenstern 1994; Kesler 1997; Barley et al. 2002; Richards 2003a, 2009; Bierlein et al. 2009). The Tethyan Alpine–Himalayan Belt stands as one of the best examples of such an orogenic system, with a large endowment of magmatic-hydrothermal ore deposits including porphyry Cu ± Mo ± Au and epithermal Au–Ag deposits (Janković 1977; Richards 2003b; Hou and Cook 2009; Yiğit 2009).

The recently discovered (in 1998) Çöpler gold deposit is located ~120 km southwest of the city of Erzincan in central eastern Turkey (Fig. 1). The deposit consists of early, low-grade porphyry-type Cu–Au mineralization overprinted by intermediate-sulfidation epithermal-style Au mineralization. Çöpler is the first significant gold discovery in eastern Anatolia, a region which had remained mostly unexplored

Published online: 20 October 2012

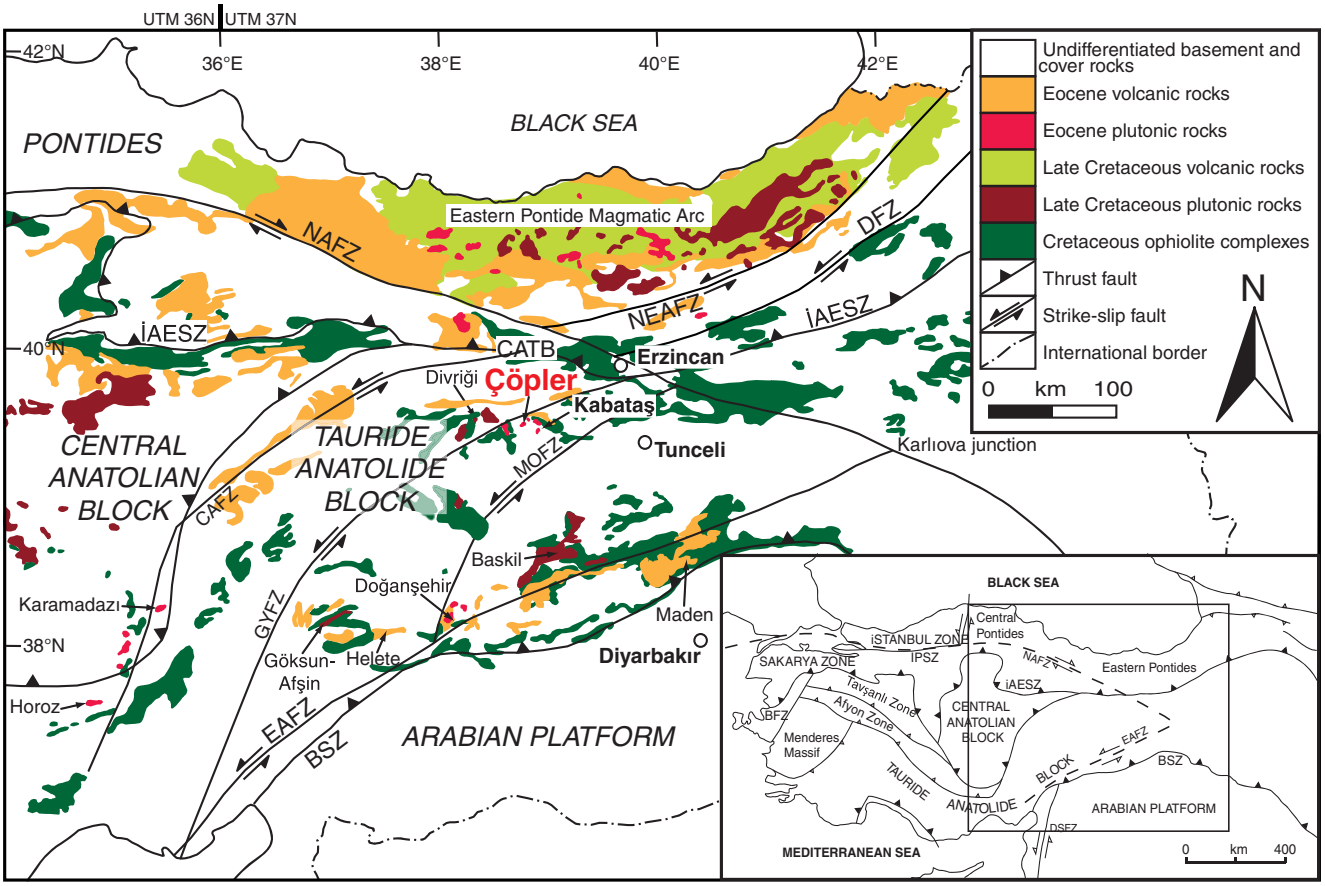

Fig. 1 Simplified geological map showing the distribution of Late Cretaceous to Eocene magmatic rocks and Cretaceous ophiolite complexes of eastern Anatolia (modified from MTA 1989, and Bozkurt 2001). *Areas shown in white* represent undifferentiated Paleozoic–Mesozoic basement rocks and Tertiary sedimentary/volcanic cover. Karlıova junction marks the intersection of the North and East Anatolian Fault Zones. *Box* shows area of Fig. 2; *inset map* shows the major tectonic elements of Turkey (Okay and Tüysüz 1999). Abbreviations: *BFZ* Bornova Flysch Zone, *BSZ* Bitlis Suture Zone, *CAFZ* Central Anatolian Fault Zone, *CATB* Central Anatolian Thrust Belt, *DFZ* Dumlu Fault Zone, *DSFZ* Dead Sea Fault Zone, *EAFZ* East Anatolian Fault Zone, *GYFZ* Göksu–Yazyurdu Fault Zone; *İAESZ* İzmir–Ankara–Erzincan Suture Zone, *IPSZ* Intra-Pontide Suture Zone, *MOFZ* Malatya–Ovacık Fault Zone, *NAFZ* North Anatolian Fault Zone, *NEAFZ* North East Anatolian Fault Zone

prior to the late 1990s. With proven and probable reserves of 4.4 million ounces (Moz) Au equivalent (95.4 million metric tonnes at 1.4 g/t Au; http://www.alacergold.com), Çöpler currently ranks as the second largest gold deposit in Turkey after the Kışladağ porphyry Au deposit in western Anatolia (430 million metric tonnes at 0.74 g/t Au; http://www.eldoradogold.com).

Porphyry-epithermal mineralization at Çöpler is spatially associated with the middle Eocene calc-alkaline Çöpler–Kabataş intrusive complex, which was emplaced into a narrow structural corridor along the northern flank of the eastern Taurus mountain range. The magmatic complex lies on the northeastern margin of the Tauride-Anatolide orogenic block (TAB), within a region of structural complexity where the modern Eurasia–Arabia collision zone is juxtaposed against at least two different suture zones marking the closure of former Neotethyan ocean basins (Figs. 1 and 2). During the Late Mesozoic–Cenozoic, basin closure along both margins of the TAB was accompanied by northward subduction and continental arc magmatism. This was followed by Late Cretaceous collision in the Pontides, and protracted periods of subduction-related and postsubduction magmatism from the middle Eocene onwards.

Although these regional magmatic and tectonic events have been the subject of several studies, understanding the geotectonic significance of the Çöpler–Kabataş magmatic complex and nearby igneous rocks of similar age and chemistry has been hindered by a lack of geological and geochronological data. The distal positioning of these intrusive centers relative to the established Late Cretaceous–Eocene arc magmatic belts in the Pontides and in southeast Anatolia (Baskil–Maden; Fig. 1) has led to conflicting interpretations regarding the nature and source of magmatism. Proposed models for the Eocene central eastern Tauride magmatic belt have ranged from typical continental arc settings (Özer and Öner 1999) to postcollisional tectonic settings in which

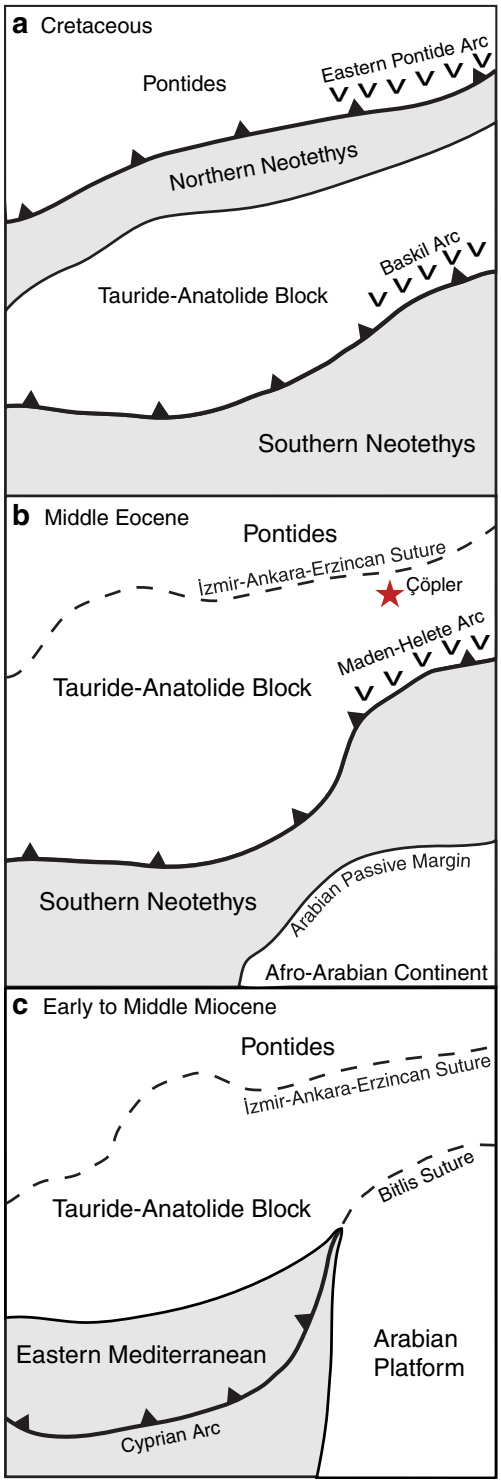

Fig. 2 Simplified sketch diagram showing the Neotethyan evolution of the Tauride-Anatolide Block and traces of Neotethyan suture zones from **a** Cretaceous to **b** Middle Eocene, to **c** Miocene times. Also shown are the approximate locations of the Çöpler deposit and the magmatic arcs that are referred in the text. Note the southward jump of the southern Neotethyan subduction zone during the Miocene (as shown in **c**)

magmatism was induced by slab steepening and break-off either (1) along the northern margin of the TAB (Önal et al. 2005) or (2) along the southern margin of the Tauride-Anatolide Block (Kuşcu et al. 2007, 2010).

This contribution provides new data on the age, geology, and geochemistry of the Çöpler–Kabataş magmatic complex and associated porphyry deposit, in order to place it more clearly in a regional tectonomagmatic and metallogenic context.

Tectonic Framework of Central Turkey

Turkey forms part of the extensive Alpine–Himalayan Orogenic Belt that stretches from SW Europe to SE Asia and is comprised largely of an assemblage of continental fragments of Tethyan origin. These continental fragments, once separated by Neotethyan basins, were amalgamated during convergence between the Eurasian and Afro-Arabian plates since at least late Mesozoic times (Fig. 2).

The ~1500-km-long TAB, which hosts the Çöpler gold deposit, is the largest of these continental fragments. During the Late Permian–Early Triassic, the TAB and other Cimmerian continents (including the laterally adjacent Central Iranian Block) started to detach from the northern Gondwana margin, initiating the southern Neotethys Ocean basin (Şengör and Yılmaz 1981; Robertson and Dixon 1984; Stampfli et al. 1991). Closure of this ocean basin commenced in the Early Cretaceous by north-dipping subduction along the Bitlis Suture (Fig. 2), accompanied by continental arc development (~88–73 Ma) along the active southern margin of the TAB (Baskil and Göksun-Afşin arcs, Fig. 1; Şengör and Yılmaz 1981; Yazgan and Chessex 1991; Yılmaz 1993; Rızaoğlu et al. 2009). At the end of the Mesozoic, subduction-related calc-alkaline magmatic activity in the TAB was interrupted, possibly due to a decrease in the rate of convergence between Arabia and Eurasia (Dewey et al. 1989) or roll-back of the southern Neotethys slab (Robertson et al. 2007; Kaymakçı et al. 2010). This subsequently led to widespread back-arc extension in the central and eastern part of the TAB. In the Eocene, arc magmatism along this margin resumed with eruption of the mafic-to-intermediate composition Maden-Helete lavas, while back-arc magmatism occurred intermittently along ENE-trending transcurrent fault systems throughout the central and eastern Taurides (Fig. 1; Yazgan 1984; Yılmaz 1993; Yiğitbaş and Yılmaz 1996a; Elmas and Yılmaz 2003; Robertson et al. 2007). The Çöpler–Kabataş intrusive complex was formed during this period in the TAB. Final closure of the southern Neotethys Ocean along the Bitlis Suture took place during the Miocene, when the Arabian Platform collided with the TAB, which by this time was already part of the southern Eurasian margin (Dewey et al. 1986; Şengör and Yılmaz 1981; Yiğitbaş and Yılmaz 1996b; Okay et al. 2010).

Contemporaneous with development of the southern Neotethys Ocean in the Early Mesozoic, a back-arc basin

known as the İzmir–Ankara–Erzincan Ocean (or northern Neotethys; Fig. 2) was formed to the north of the TAB (Robertson and Pickett 2000; Stampfli 2000; Tekin et al. 2002; Okay et al. 2006). This short-lived basin was closed in the Cretaceous, first by intra-oceanic subduction of unknown polarity, and then by northward subduction beneath the Eurasian margin to form the Eastern Pontide Magmatic Arc (Figs. 1 and 2). Collision between the Pontides and the TAB occurred in the Late Cretaceous, with obduction of ophiolites onto the north-facing margin of the TAB (Figs. 1 and 2; Okay and Şahintürk 1997; Rice et al. 2006; Tüysüz and Tekin 2007).

In the Paleocene, continued N–S-directed convergence along the collisional belt resulted in transpressional deformation of the eastern Pontides, accompanied by folding, thrusting, and uplift (Okay and Şahintürk 1997; Kaymakçı et al. 2000). Collapse of the crustally thickened orogen occurred during the middle Eocene, initiating an episode of postcollisional calc-alkaline magmatism (50–41 Ma) mainly within ENE- and E–W-trending extensional basins in the Pontides, and along the İzmir–Ankara–Erzincan Suture Zone (Fig. 1; Okay and Şahintürk 1997; Topuz et al. 2005; Keskin et al. 2008).

The Miocene collision of Eurasia and Arabia along the Bitlis Suture heralded the start of continent–continent (as opposed to microplate–continent) collision in this region. Collision was followed by uplift and extensive deformation of eastern Anatolia and by westward migration of the main Anatolian Block along two new regional strike-slip structures, the North and East Anatolian Fault Zones. These faults are roughly concurrent with the pre-existing Neotethyan sutures (Fig. 1; Dewey et al. 1986). Widespread postcollisional volcanism occurred throughout Anatolia from the Miocene onwards. In eastern Anatolia, it has been suggested that this volcanic activity was associated either with delamination of the subcontinental lithospheric mantle (Pearce et al. 1990; Göğüş and Pysklywec 2008) or with slab steepening and break-off following collision (Keskin 2003; Şengör et al. 2003; Faccenna et al. 2006; Lei and Zhao 2007). In contrast, in western Anatolia, this volcanism is attributed to Miocene to Recent extensional tectonics related to the opening of the Aegean back-arc (McKenzie and Yılmaz 1991).

Regional Geological and Structural Setting of the Tauride-Anatolide Block

The eastern part of the TAB consists of a number of tectonomagmatic and stratigraphic units including the Paleozoic–Mesozoic Keban metamorphic massif, the Munzur allochthon (Late Triassic–Cretaceous platform and deep marine carbonates), Cretaceous ophiolite complexes, Late Cretaceous and Cenozoic igneous rocks, and Cenozoic sedimentary cover rocks of the Sivas Basin; Fig. 3; Michard et al. 1984; Özgül and Turşucu 1984; Özer 1994). The Munzur allochthon was overthrust onto the Permo–Triassic metamorphic basement in the Late Cretaceous (Özgül and Turşucu 1984), forming an extensive east–west-trending mountain range between Tunceli to the south and Erzincan to the north (Fig. 1). The steep topography of the allochthon gradually diminishes outwards towards the surrounding Late Cretaceous–Tertiary sedimentary basins.

The Munzur allochthon comprises a thick succession of deep marine and platform-type carbonate rocks (Özgül and Turşucu 1984; Tunç et al. 1991). Its northern flank has been extensively overlain by tectonic slivers of Cretaceous ophiolitic rocks and melange that were accreted during Late Cretaceous dextral transpression associated with closure of the İzmir–Ankara–Erzincan ocean basin (Özgül et al. 1981; Yılmaz 1985; Kaymakçı et al. 2000; Yalınız et al. 2000; Okay et al. 2001). Both carbonate rocks and obducted ophiolites were later intruded and covered by igneous rocks of varying composition during three distinct magmatic episodes: an early bimodal alkaline intrusive event during the Late Cretaceous, a more voluminous calc-alkaline intrusive and extrusive event in the Eocene, and a widespread bimodal volcanic event in the Miocene.

The oldest magmatic phase in the vicinity of the Munzur allochthon is represented by sporadic exposures of Late Cretaceous bimodal intrusions including the Murmano and Dumluca plutons near Divriği, and several small intrusive centers located near Hekimhan (Figs. 1 and 3). Intrusive rocks of this stage are typically alkaline syenite-quartz monzonite and diorite-gabbro suites with ages between ~76 and 74 Ma (Zeck and Ünlü 1991; Yılmaz et al. 1993; Kadıoğlu et al. 2006; Boztuğ et al. 2007; Kuşcu et al. 2007, 2010; Marschik et al. 2008; Özgenç and İlbeyli 2009; this study). Emplacement of these bimodal plutons seems to coincide with break-up and collapse of the thickened eastern TAB crust, the result of which was a reversal in stress directions and a switch from transpression to transtension. From Late Cretaceous until middle Eocene time, this transtensional period led to the opening of several ENE-trending foreland-type sedimentary basins (Cater et al. 1991; Temiz et al. 1993), and exhumation of metamorphic complexes (Gautier et al. 2002; Umhoefer et al. 2007; Whitney et al. 2008), mainly along Cretaceous thrust fault systems reactivated as sinistral strike-slip faults (Figs. 1 and 3; Koçyiğit and Beyhan 1998; Poisson et al. 1996; Fayon et al. 2001).

Eocene magmatic rocks are widely scattered throughout the northeastern Taurides and include the Çöpler–Kabataş magmatic complex, the Çaltı and Bizmişen plutons, and an east–west-trending belt of volcano-sedimentary rocks that crop out adjacent to the İzmir–Ankara–Erzincan Suture Zone (Figs. 1 and 3). Intrusive rocks consist of calc-alkaline diorite, quartz diorite, granodiorite, and quartz monzonite, and volcanic rocks range from basaltic andesite

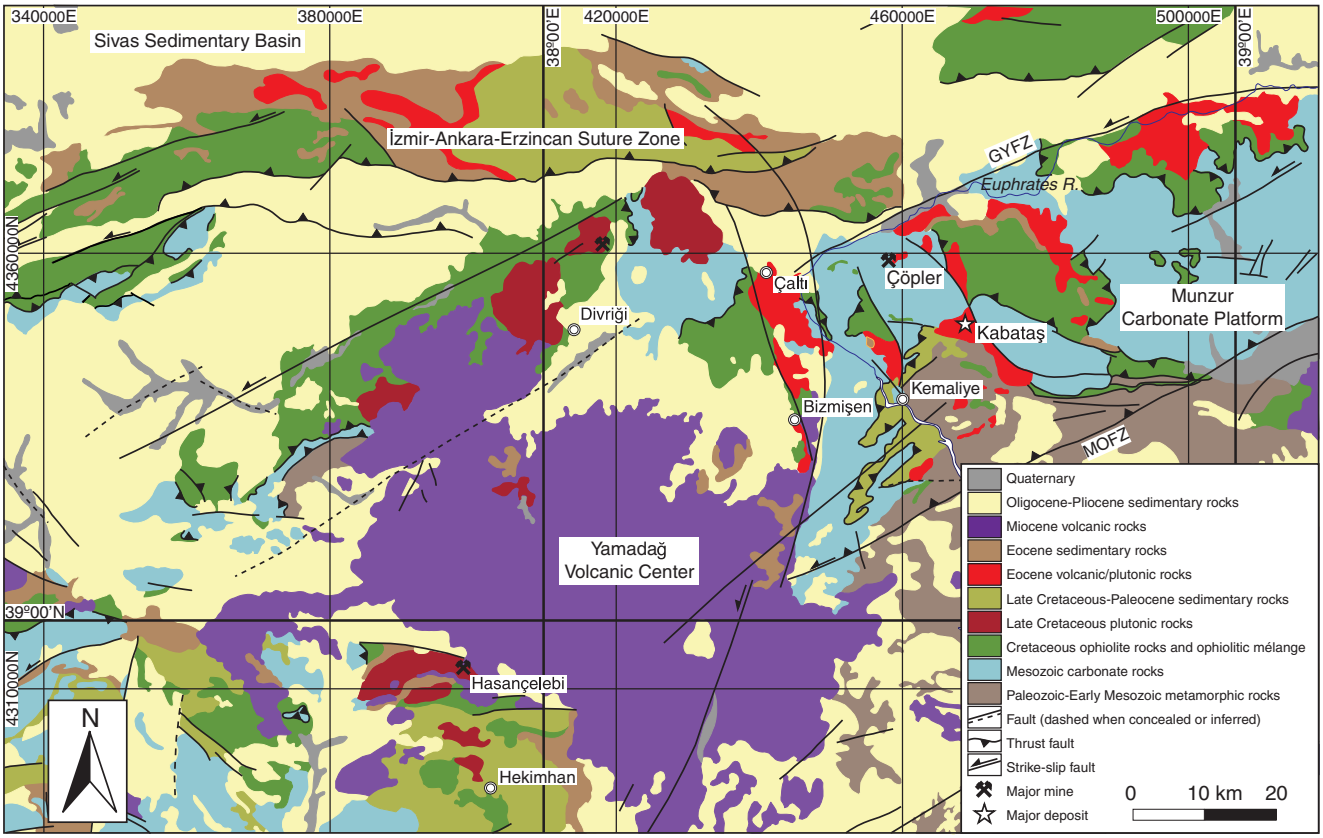

Fig. 3 Simplified geological map of the eastern Tauride-Anatolide Block. Compiled from the 1:500,000 geological map of Turkey, Sivas, and Erzurum quadrangles (MTA 2002a, b; UTM Zone 37N). Structural data are modified from Kaymakçı et al. (2006). Abbreviations: *GYFZ* Göksu–Yazyurdu Fault Zone, *MOFZ* Malatya–Ovacık Fault Zone

to rhyolite (Özer and Öner 1999; Önal et al. 2005; Kuşcu et al. 2007; Keskin et al. 2008). Although their geochemical characteristics are similar to global arc magmas, the Eocene igneous rocks do not form a continuous narrow magmatic belt as in many volcanic arcs, but rather occur as isolated intrusive and volcanic complexes localized in structurally favorable sites and distal to the presumed coeval subduction zone and arc to the south.

The Karamadazı, Horoz, and Doğanşehir plutons are other regionally significant Eocene intrusive systems, which follow the same general structural trend to the southwest (Fig. 1; see discussion below). All three plutons are reported to be Eocene in age (~50–48 Ma), and consist of felsic to intermediate subalkaline lithologies (Gençalioğlu-Kuşcu et al. 2001; Karaoğlan and Parlak 2006; Karaoğlan et al. 2009; Kadıoğlu and Dilek 2010; Kuşcu et al. 2010).

Throughout the northeastern TAB, much of the Late Cretaceous–Middle Eocene magmatism appears to have been controlled by two prominent ENE-trending structures, the sinistral Central Anatolian and Göksu–Yazyurdu Fault Zones (Fig. 1), which accommodated a component of the transtensional deformation. Shallow level pluton emplacement is favored at times of oblique transtensional or transpressional movement (e.g., Hutton 1982; 1990; Glazner 1991; Román-Berdiel et al. 1997; Tosdal and Richards 2001). During the Eocene transtensional period, a total sinistral displacement of 74 km is recorded along the Central Anatolian Fault Zone (Koçyiğit and Beyhan 1998), but the offset along the Göksu–Yazyurdu Fault Zone to the south is not known.

The northeastern TAB experienced a final stage of widespread postcollisional magmatism in the Miocene, erupted along strike-slip fault systems. For example, basaltic trachyandesite to dacite volcanic rocks form the 19–11 Ma Yamadağ volcanic center to the southwest of Çöpler (Fig. 3; Arger et al. 2000; Kürüm et al. 2008; Ekici et al. 2009). These magmas are interpreted to have formed during postcollisional readjustments by melting of subduction-modified lithospheric sources remnant from earlier Neotethyan subduction events (Arger et al. 2000; Keskin 2003; Kürüm et al. 2008; Ekici et al. 2009).

Local geological setting of the Çöpler Au deposit

The Çöpler gold deposit is located in the central eastern part of the TAB, along the northern flanks of the Munzur

Mountains, roughly 3 km southeast of the Euphrates River (Fig. 3). The deposit is spatially related to an Eocene composite stock forming the northwestern extension of the Çöpler–Kabataş magmatic complex (Figs. 4 and 5), which intruded a basement of Late Paleozoic–Cretaceous sedimentary and ophiolitic rocks (Figs. 3, 4, 5, and 6). The intrusive system at Çöpler is exposed within a 1×2 km wide, bowl-shaped, ENE-trending structural window (the Çöpler window; Figs. 4 and 5), along which block-faulted rocks have been exposed underneath the regional thrust sheet of the Munzur carbonate allochthon. The intrusive complex appears to postdate thrusting and locally intrudes the base of the thrust sheet causing contact-metamorphism to marble.

Paleozoic–Mesozoic Basement Units

The basement in the Çöpler area consists of an 800-m-thick succession of regionally metamorphosed Permo–Triassic siliciclastic sedimentary rocks, which belong to the Yoncayolu Formation of the Keban metamorphic massif (Özgül and Turşucu 1984). This unit is exposed in the western part of the Çöpler window and in the vicinity of Kabataş village (Figs. 4 and 5). The metasedimentary succession consists of uniformly alternating layers of shelf-type clastic rocks, which underwent low-grade greenschist facies metamorphism in conjunction with Late Cretaceous obduction of ophiolites onto the northern TAB margin (Özgül et al. 1981; Özgül and Turşucu 1984). These rocks are characterized by a mineral assemblage of chlorite + quartz ± sericite ± epidote; however, brown-colored biotite-rich and pale green-colored diopside-rich hornfels are locally developed at contacts with the Eocene intrusions.

Structurally overlying the metamorphic basement is the Late Triassic to Cretaceous allochthonous Munzur carbonate platform, which displays an overall younging trend from south to north (Özgül and Turşucu 1984). The northern section of this allochthon, which is exposed between Çöpler and Kabataş villages, consists of a 300-m-thick succession of Cenomanian to Campanian rudist-bearing limestones (Özgül and Turşucu 1984). The base of the

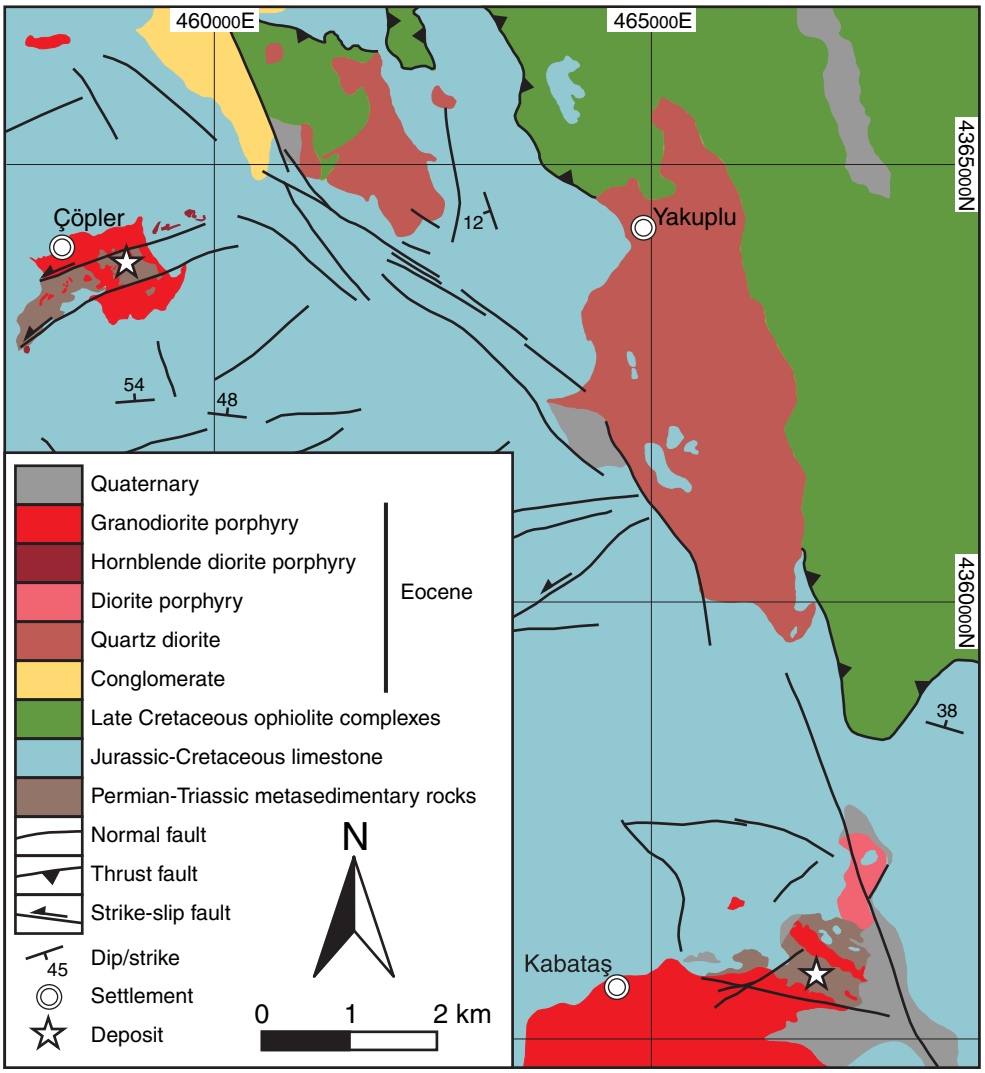

Fig. 4 Geological map of the Çöpler–Kabataş magmatic complex, modified from Özer (1994)

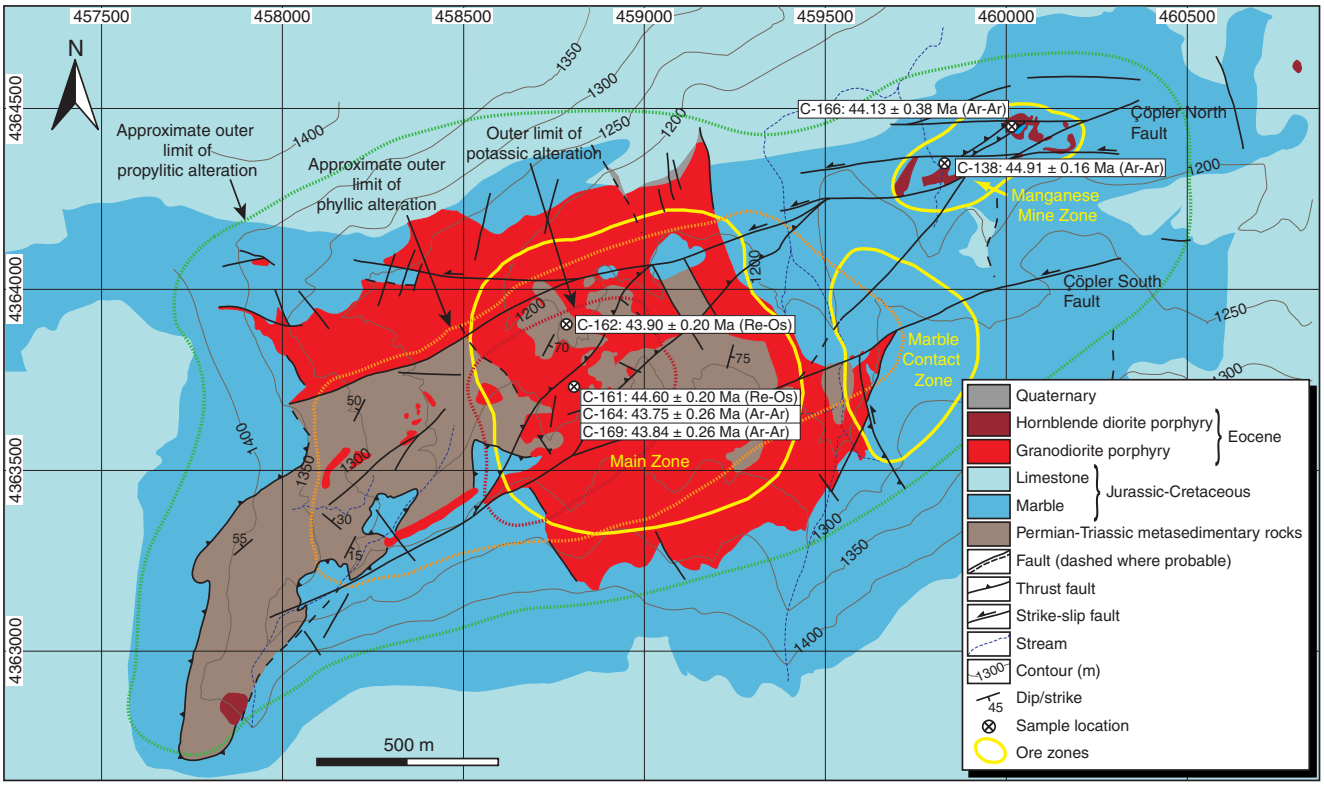

Fig. 5 Geological map of the Çöpler deposit, modified from a map prepared by Anatolia Minerals Development Limited (UTM Zone 37N). The Çöpler intrusive system is exposed in the structural window defined by the steeply-dipping Çöpler North and South Faults dissecting the Paleozoic–Mesozoic basement lithologies. The extents of the main alteration facies are outlined by surface projection of drillhole data. Also shown are the sample locations for $^{40}Ar/^{39}Ar$ and Re–Os geochronology

limestone sequence is poorly exposed, but in the southwestern sector of the Çöpler window, metasedimentary rock injections into the Munzur limestone were observed (Fig. 7a). These textures are interpreted to reflect south-

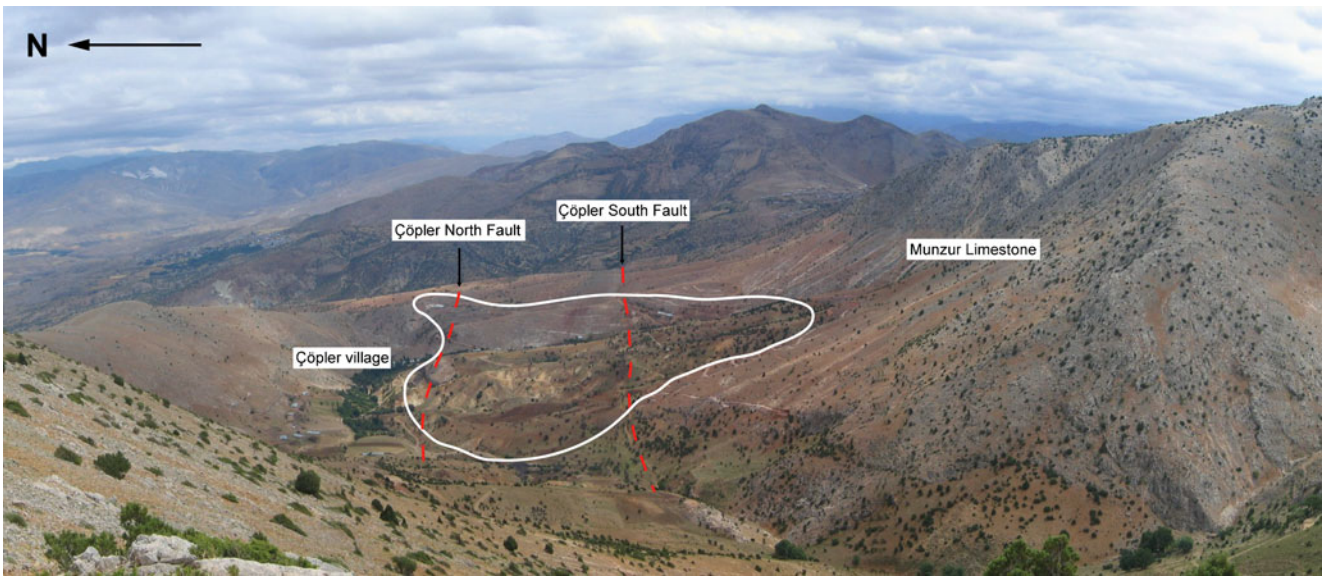

Fig. 6 Photograph showing the main Çöpler window, looking east. *Dashed red lines* indicate traces of the Çöpler North and South Faults. Also outlined is the approximate extent of the porphyry–epithermal mineralization (*white line*; ~900 m wide in this view). Resistant hills lying to the south and north of these faults are carbonate rocks of the Munzur platform. The main peak in the background (approximately 4 km to the east) is a Cretaceous ophiolite nappe thrust onto these carbonate rocks. The low-lying area in the far left (northeast) is part of the Tertiary Sivas Basin

Fig. 7 Photographs of the main lithologic units in the Çöpler–Kabataş area. **a** Permo-Triassic metasedimentary basement rocks and the overlying Munzur limestone. The contact between the two units is characterized by deformation structures with metasedimentary rock injections into the base of the overlying limestone (0457248E, 4362979N). **b** Granodiorite porphyry intrusion from the Çöpler main zone with centimeter-sized biotite-rich xenoliths (CDD-002, 293–294 m; 0458972E, 4363881N). **c** Relatively fresh hornblende diorite porphyry from the manganese mine zone (near 0460177E, 4364450N); the slightly green coloration is due to weak propylitic alteration of the matrix. **d** Weakly propylitized quartz diorite containing hornblende-plagioclase-rich xenoliths, exposed approximately 1 km to the east of the Çöpler area (0461485E, 4365002N)

vergent décollement thrusting of the carbonate platform during the Campanian–Maastrichtian interval (Özgül et al. 1981; Özgül and Turşucu 1984). The limestones are metamorphosed to sugary-textured white marble for several hundred meters around the intrusive contacts (Fig. 5).

The Eocene Çöpler–Kabataş Magmatic Complex

The Çöpler–Kabataş magmatic complex intrudes the Paleozoic–Mesozoic basement and overlying limestones as several stocks that range in width from a few hundred meters to several kilometers (Fig. 4). The intrusive rocks are porphyritic to equigranular and intermediate composition, with ubiquitous and abundant plagioclase (andesine). Quartz is also a common constituent of many of these igneous lithologies, whereas K-feldspar was not observed in unaltered rocks. Green-colored hornblende is the predominant mafic phase and is present in most igneous lithologies, whereas biotite and clinopyroxene are sparse.

Granodiorite porphyry The predominant phase in the Çöpler–Kabataş magmatic complex is a granodiorite porphyry that crops out in the main Çöpler window (Figs. 4 and 5) and also near Kabataş village (Fig. 4). At Çöpler, this unit is mainly exposed between the Çöpler North and South Faults and also occurs as two lobes to the north and south of these structures (Fig. 5). Granodiorite porphyry contains abundant plagioclase, hornblende, and sparse biotite phenocrysts set in a fine-grained groundmass of plagioclase, quartz, and lesser magnetite (Figs. 7b and 8a). Euhedral to subhedral phenocrysts, ranging in size from 0.5 to 4 mm, make up to about 70 vol% of the rock. Rounded, biotite-rich mafic xenoliths are occasionally present in the granodiorite porphyry (Fig. 7b). Both in Çöpler and Kabataş, granodiorite porphyry has undergone widespread hydrothermal alteration, and its least-altered varieties display weak propylitic alteration with partial replacement of mafic phases by chlorite and epidote, together with sparse carbonate.

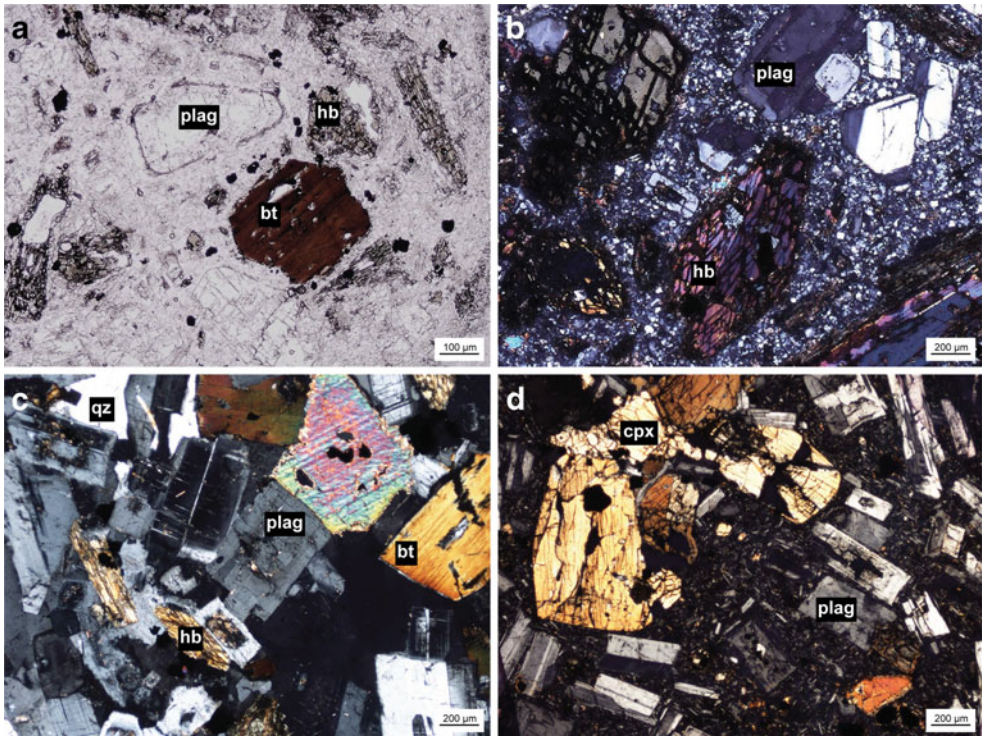

Fig. 8 Photomicrographs in **a** plane- and **b**–**d** cross-polarized light of intrusive rocks from the Çöpler–Kabataş Magmatic Complex. **a** Granodiorite porphyry from the Çöpler main zone, with biotite, hornblende, and plagioclase phenocrysts, set in a groundmass of quartz, plagioclase, and magnetite (sample C-164; CDD-140, 106 m; 0458723E, 4363842N). **b** Hornblende diorite porphyry from the Çöpler manganese mine zone, with large hornblende and plagioclase phenocrysts, set in a quartzofeldspathic groundmass (sample C-166; CDD-159, 26 m; 0460072E, 4364353N). **c** Equigranular quartz diorite from east of the Çöpler window, with abundant plagioclase, biotite, and lesser quartz and hornblende (sample CR-02; 0464761E, 4362274N). **d** Clinopyroxene-bearing diorite porphyry from near Kabataş, with abundant plagioclase and glomeroporphyritic clinopyroxene phenocrysts, set in a glassy groundmass containing plagioclase microcrysts (sample CR-03; 0467648E, 4362274N)

Hornblende diorite porphyry Hornblende diorite porphyry is exposed as several small stocks in the northeast and southwest sectors of the Çöpler window, in close association with east–west-trending structures (Figs. 5 and 7c). The hornblende diorite porphyry contains abundant plagioclase and hornblende phenocrysts within a fine-grained plagioclase–quartz–magnetite groundmass, with a significantly lower phenocryst to groundmass ratio than the granodiorite porphyry (Fig. 8b). Its relationship with the granodiorite porphyry is unclear because it has mostly been intensely altered. Least-altered samples of hornblende diorite porphyry exhibit weak propylitic alteration as indicated by partial replacement of hornblende by chlorite and by the presence of sparse epidote and carbonate in the groundmass.

Quartz diorite Quartz diorite occurs as NW-oriented lensoidal bodies to the east of Çöpler, along the eastern side of a NNW-trending structure (Fig. 4). This unit, previously named the Yakuplu Pluton (Özer 1994; Özer and Öner 1999), consists of medium-grained, subhedral to euhedral phenocrystic quartz, plagioclase, biotite, and hornblende, with minor magnetite (Figs. 7d and 8c). Similar to the granodiorite porphyry, quartz diorite also commonly contains mafic enclaves (Fig. 7d). The quartz diorite exhibits weak propylitic alteration readily recognized by crosscutting veinlets of epidote, and mafic phenocrysts partially rimmed by chlorite along with lesser amounts of epidote and carbonate.

Diorite porphyry A relatively small stock of diorite porphyry occurs to the northeast of Kabataş (Fig. 4). The diorite porphyry is unaltered and consists of phenocrystic plagioclase and clinopyroxene, in a groundmass of plagioclase microcrysts and substantial amounts of magnetite (Fig. 8d). Euhedral plagioclase phenocrysts (0.1–0.5 mm) display either polysynthetic twinning or oscillatory zoning, whereas clinopyroxene phenocrysts (0.2–0.5 mm) commonly occur in glomeroporphyritic clusters.

Structure

The Çöpler intrusive system and the underlying basement sequence are disrupted by several sets of high-angle faults. The predominant structural features within the Çöpler

window are the ENE-trending Çöpler North and South Faults that are related to Late Cretaceous–Eocene sinistral deformation along the regional Göksu–Yazyurdu Fault Zone (Fig. 5). NE–SW-trending extensional structures linking the ENE-trending faults and E–W-trending sinistral faults also developed in relation to middle Eocene transtensional deformation, and facilitated shallow level magma emplacement and hydrothermal mineralization at Çöpler. The NE–SW-trending structures were later reactivated as reverse faults during later minor contractional deformation. A fourth set of NNW-trending faults truncates the granodiorite porphyry, and locally offsets the earlier fault sets. All structures at Çöpler have been reactivated on several occasions as evidenced by postemplacement faulting and brecciation (Fig. 5).

Porphyry Cu–(Au) and epithermal Au mineralization and alteration at Çöpler

A brief account of the alteration and mineralization styles at Çöpler is provided below as a context for the geochronological data. A more detailed account will appear in a later publication that focuses on ore formation.

Low-grade porphyry Cu–Au and superimposed epithermal Au mineralization occur in three different zones at Çöpler: the Main Zone, the Marble Contact Zone, and the Manganese Mine Zone (Fig. 5). Each zone displays distinct hydrothermal alteration and mineralization features. The Main Zone is characterized by high-temperature porphyry-style alteration and Cu–(Au) mineralization centered around the granodiorite porphyry. Here, early potassic alteration, consisting of hydrothermal biotite and K-feldspar, forms an inner core with associated quartz–magnetite–chalcopyrite–pyrite ± molybdenite veinlets. The central potassic alteration zone grades outwards into a laterally more extensive phyllic alteration zone, which is readily distinguished by pervasive sericite–quartz alteration and stockwork quartz–pyrite veinlets. Both alteration styles are enveloped by a propylitic alteration assemblage of chlorite–epidote–carbonate developed peripheral to the Main Zone.

Epithermal-style mineralization is locally superimposed on the early porphyry-style mineralization within the Main Zone, but is best developed in the Marble Contact and Manganese Mine Zones. The Marble Contact Zone is proximal to the Main Zone and occupies the southeast margin of the granodiorite porphyry, whereas the Manganese Mine Zone is delimited by two E–W-trending secondary fault systems and related extensional structures in the northeastern sector of the property (Fig. 5). Both zones consist of Au-bearing quartz–carbonate–sulfide ± barite veins and Au-bearing manto-type carbonate replacement bodies of massive sulfides along the basal contact of the Munzur limestone, which have largely been oxidized to gossan, particularly in the Manganese Mine Zone. In these oxidized zones, hypogene Mn carbonates (rhodochrosite or manganocalcite) have been altered to manganese wad.

Sampling and analytical methods

Sample selection

Samples for petrographic, whole-rock geochemical, and geochronological analysis were collected from diamond drill core at the Çöpler deposit, and outcrop exposures within or nearby the Çöpler–Kabataş magmatic complex. A summary of sample descriptions and locations is provided in the Electronic Supplementary Material (ESM 1).

Twelve drill core and outcrop samples of least-altered (6) and altered (6) igneous rocks from the Çöpler–Kabataş magmatic complex were analyzed for their major and trace element compositions. In addition, nine other samples of fresh igneous rocks from elsewhere across the central eastern Taurides were collected and analyzed for comparison purposes. Five of these regional samples were obtained from Eocene intrusions near Bizmişen, Çaltı, Doğanşehir, Horoz, and Karamadazı (Figs. 1 and 3), three samples were collected from Late Cretaceous intrusions near Divriği, and one sample was collected from the Miocene Yamadağ volcanic center to the south of Divriği.

Altered samples from the Çöpler–Kabataş magmatic complex contain either an overprinting propylitic alteration assemblage of chlorite, epidote, and carbonate, or a phyllic alteration assemblage consisting of sericite replacing mafic minerals and plagioclase, as reflected in their relatively high loss-on-ignition values (Table 1).

Three samples containing igneous biotite and/or hornblende were selected for $^{40}Ar/^{39}Ar$ incremental step-heating analysis from a suite of least-altered plutonic rocks from the Çöpler–Kabataş magmatic complex. Two potassic (biotite) and phyllic (sericite) altered samples were also analyzed to constrain the timing of hydrothermal alteration related to porphyry mineralization at Çöpler. In addition, three samples of fresh rock containing igneous biotite and/or hornblende were selected from the Bizmişen, Çaltı, and Divriği intrusions in order to constrain the timing of intrusive magmatism elsewhere in the central eastern Taurides.

In order to constrain the timing of porphyry-style mineralization, two molybdenite samples obtained from quartz–magnetite–sulfide veinlets within the Çöpler Main Zone were analyzed by the Re–Os method.

Whole-rock geochemistry

Sample preparation and whole-rock geochemical analyses of 21 igneous rock samples were carried out at Actlabs

Table 1 Major and trace element analyses of least-altered and altered igneous rocks from the Çöpler–Kabataş magmatic complex and least-altered igneous lithologies from the surrounding area

Location		Çöpler–Kabataş											Divriği			Yamadağ	Çaltı	Bizmişen	Çöpler–Kabataş	Doğanşehir	Karamadazı	Horoz
Sample no.		C-014	C-104	C-163	C-164	C-166	C-169	C-173	CR-01	CR-02	CR-03	CR-05	CR-07	CR-08	CR-09	CR-10	CR-11	CR-12	CR-14	CR-24	CR-28	CR-31
Lithology[a]		Hbl Diorite Porphyry	Grd. Porphyry	Grd. Porphyry	Grd. Porphyry	Hbl Diorite Porphyry	Grd. Porphyry	Grd. Porphyry	Quartz Diorite	Quartz Diorite	Diorite Porphyry	Quartz Diorite	Quartz Monzonite	Quartz Monzonite	Alk. Feld. Granite	Basaltic Andesite	Tonalite	Diorite	Hbl Diorite Porphyry	Tonalite	Granite	Granite
Alteration		Least-alt.	Least-alt.	Alt. (prop)	Alt. (prop)	Alt. (prop)	Alt. (K)	Least-alt.	Least-alt.	Least-alt.	Least-alt.	Alt. (phyl)	Least-alt.	Least-alt.	Least-alt.	Least-alt.	Least-alt.	Least-alt.	Alt. (prop)	Least-alt.	Least-alt.	Least-alt.
Weight %	Method (detection limit)																					
SiO_2	Fusion-ICP (0.01)	64.05	64.44	59.01	60.63	54.29	62.69	65.25	67.50	65.75	57.11	62.58	62.98	65.10	72.04	55.11	65.19	54.92	54.23	65.91	76.48	73.11
Al_2O_3	Fusion-ICP (0.01)	15.98	16.37	16.06	16.64	16.30	16.48	15.88	65.75	16.13	17.73	15.53	16.36	17.16	14.04	16.26	15.84	16.46	16.11	16.47	12.20	14.38
$Fe_2O_{3(T)}$	Fusion-ICP (0.01)	4.79	4.01	5.37	4.15	4.78	4.44	4.20	3.59	4.33	6.96	3.89	4.26	2.70	1.50	8.21	4.32	8.95	5.20	4.08	0.90	2.05
MnO	Fusion-ICP (0.001)	0.10	0.06	0.03	0.09	0.24	0.04	0.05	0.05	0.07	0.08	0.14	0.06	0.03	0.02	0.13	0.05	0.15	0.03	0.01	0.03	0.01
MgO	Fusion-ICP (0.01)	1.74	1.76	2.50	1.55	0.91	1.99	1.53	1.64	1.74	2.36	1.12	1.64	0.16	0.13	4.87	1.68	4.11	1.80	1.74	0.08	0.67
CaO	Fusion-ICP (0.01)	5.11	3.61	4.44	5.54	11.30	4.26	3.90	3.98	4.68	7.30	4.71	3.64	2.34	0.47	7.71	4.66	8.20	11.19	4.52	0.66	2.18
Na_2O	Fusion-ICP (0.01)	3.37	3.02	1.76	2.50	2.65	2.78	2.85	3.50	3.60	3.36	2.92	4.23	4.97	3.88	3.78	3.51	3.59	2.57	4.33	3.30	3.82
K_2O	Fusion-ICP (0.01)	3.05	3.50	2.75	2.82	2.98	3.46	3.11	2.44	2.20	1.76	3.21	4.37	5.46	6.05	1.14	2.27	1.77	4.09	1.76	4.72	3.52
TiO_2	Fusion-ICP (0.001)	0.46	0.41	0.532	0.54	0.55	0.52	0.44	0.35	0.43	0.78	0.36	0.57	0.41	0.18	1.17	0.41	0.95	0.59	0.46	0.09	0.22
P_2O_5	Fusion-ICP (0.01)	0.21	0.18	0.24	0.26	0.25	0.23	0.19	0.11	0.15	0.16	0.16	0.25	0.10	0.02	0.20	0.15	0.18	0.26	0.15	0.03	0.11
LOI	Fusion-ICP (0.01)	1.61	2.77	6.50	5.18	6.65	3.90	3.30	1.19	0.85	1.45	4.49	0.45	1.83	0.71	0.61	1.09	0.89	4.59	0.81	0.25	0.64
Total		100.50	100.10	99.18	99.91	100.90	100.80	100.70	100.30	99.94	99.05	99.11	98.82	100.3	99.02	99.19	99.18	100.20	100.70	100.20	98.72	100.70
ppm (except unless indicated)																						
Au (ppb)	INAA (1)	42	17	53	70	8	138	14	<d.l.	<d.l.	<d.l.	2	<d.l.	1	6	<d.l.	<d.l.	<d.l.	6	<d.l.	<d.l.	<d.l.
Ag	MULT INAA/TD-ICP-MS (0.5)	<d.l.	<d.l.	<d.l.	<d.l.	<d.l.	<d.l.	<d.l.	<d.l.	<d.l.	<d.l.	<d.l.	<d.l.	<d.l.	<d.l.	<d.l.	<d.l.	<d.l.	<d.l.	<d.l.	<d.l.	<d.l.
As	INAA (1)	2	2	<d.l.	14	8	3	6	<d.l.	<d.l.	<d.l.	2	3	7	8	<d.l.	<d.l.	<d.l.	8	<d.l.	<d.l.	2
Ba	Fusion-ICP (1)	771	717	561	634	762	691	736	623	665	290	571	983	547	108	245	708	464	836	733	125	534
Be	Fusion-ICP (1)	2	2	2	2	2	2	2	1	1	1	2	5	7	6	2	1	1	3	3	3	3
Bi	Fusion-ICP-MS (0.1)	0.1	0.1	0.1	0.2	0.3	0.4	0.1	0.1	2.7	0.3	0.3	0.2	0.4	0.3	<d.l.	0.1	0.3	<d.l.	<d.l.	<d.l.	<d.l.
Br	INAA (0.5)	<d.l.	0.9	<d.l.	<d.l.	1	<d.l.	1.3	<d.l.	1	1.1	<d.l.	<d.l.	1.4	2.1	<d.l.	<d.l.	1.3	<d.l.	<d.l.	1	<d.l.
Cd	TD-ICP (0.5)	<d.l.	<d.l.	<d.l.	0.5	<d.l.	<d.l.	<d.l.	<d.l.	<d.l.	<d.l.	<d.l.	<d.l.	<d.l.	<d.l.	0.5	<d.l.	<d.l.	<d.l.	<d.l.	<d.l.	<d.l.
Co	INAA (0.1)	9.2	5	10	10.6	16.9	10	7.1	7.4	8.7	15.7	8.6	7.8	2.9	2.5	31.3	8.8	21.8	14	8	3	5
Cr	INAA (0.5)	10.8	7.7	8.2	6.6	<d.l.	5.5	5.6	9.5	13.5	5.7	13.6	14.9	4.8	6.7	135	14.5	22.7	29	61	66	26
Cs	Fusion-ICP-MS (0.1)	0.4	1.1	2.3	4.1	1.6	1.9	1.5	0.9	0.9	0.6	1.1	2.3	3.5	3.2	2.1	0.7	1	0.9	0.2	2.2	1
Cu	TD-ICP (1)	185	149	561	221	20	734	246	143	26	23	40	9	9	9	38	9	14	33	13	4	3
Ga	Fusion-ICP-MS (1)	18	17	16	16	17	18	17	14	16	19	16	19	23	22	17	15	17	17	17	11	16
Ge		1.6	1.5	1.3	0.9	0.9	1.7	1.6	1.4	1.5	1.4	1.4	1.3	1.4	1.4	1.1	1.4	1.5	1.2	1.3	1.7	1.2

Table 1 (continued)

Location		Çöpler–Kabataş											Divriği			Yamadağ	Çaltı	Bizmişen	Çöpler–Kabataş	Doğanşehir	Karamadazı	Horoz
Sample no.		C-014	C-104	C-163	C-164	C-166	C-169	C-173	CR-01	CR-02	CR-03	CR-05	CR-07	CR-08	CR-09	CR-10	CR-11	CR-12	CR-14	CR-24	CR-28	CR-31
Lithology[a]		Hbl Diorite Porphyry	Grd. Porphyry	Grd. Porphyry	Grd. Porphyry	Hbl Diorite Porphyry	Grd. Porphyry	Grd. Porphyry	Quartz Diorite	Quartz Diorite	Diorite Porphyry	Quartz Diorite	Quartz Monzonite	Quartz Monzonite	Alk. Feld. Granite	Basaltic Andesite	Tonalite	Diorite	Hbl Diorite Porphyry	Tonalite	Granite	Granite
Alteration		Least-alt.	Least-alt.	Alt. (prop)	Alt. (prop)	Alt. (prop)	Alt. (K)	Least-alt.	Least-alt.	Least-alt.	Least-alt.	Alt. (phyl)	Least-alt.	Least-alt.	Least-alt.	Least-alt.	Least-alt.	Least-alt.	Alt. (prop)	Least-alt.	Least-alt.	Least-alt.
	Fusion-ICP-MS (0.5)																					
Hf	Fusion-ICP-MS (0.1)	3.3	3.1	2.7	3.1	2.8	3.3	3.6	2.9	3	3.7	3.2	6.5	10.7	5.4	3.2	2.8	3.3	2.8	3.5	4.5	3
Hg	INAA (1)	<d.l.	<d.l.	<d.l.	<d.l.	<d.l.	<d.l.	<d.l.	<d.l.	<d.l.	<d.l.	<d.l.	<d.l.	<d.l.	<d.l.	<d.l.	<d.l.	<d.l.	<d.l.	<d.l.	<d.l.	<d.l.
In	Fusion-ICP-MS (0.1)	<d.l.	<d.l.	<d.l.	<d.l.	<d.l.	<d.l.	<d.l.	<d.l.	<d.l.	<d.l.	<d.l.	<d.l.	<d.l.	<d.l.	<d.l.	<d.l.	<d.l.	<d.l.	<d.l.	<d.l.	<d.l.
Ir (ppb)	INAA (1)	<d.l.	<d.l.	<d.l.	<d.l.	<d.l.	<d.l.	<d.l.	<d.l.	<d.l.	<d.l.	<d.l.	<d.l.	<d.l.	<d.l.	<d.l.	<d.l.	<d.l.	21	<d.l.	<d.l.	<d.l.
Nb	Fusion-ICP-MS (0.2)	8.6	8.3	6.9	8.7	7.1	8.1	8.4	6.4	6.8	5.4	8.3	21	71.5	54.8	6.8	7.4	7.2	7.4	13.1	26.3	12.3
Ni	TD-ICP (1)	3	3	3	74	96	21	22	3	5	3	8	5	1	1	45	5	5	5	9	4	4
Pb	TD-ICP (5)	9	9	8	37	10	<d.l.	5	7	7	7	13	12	11	7	10	7	7	17	<d.l.	6	<d.l.
Rb	Fusion-ICP-MS (2)	63	76	66	83	68	101	91	62	61	40	49	167	218	308	36	54	36	82	36	190	80
S (%)	TD-ICP (0.001)	0.26	0.49	0.59	1.75	1.86	0.76	0.315	0.013	0.002	<d.l.	0.016	<d.l.	0.002	0.003	0.003	0.002	0.052	0.62	0.006	0.002	0.001
Sb	INAA (0.1)	<d.l.	0.5	<d.l.	1	0.8	0.3	0.3	<d.l.	<d.l.	0.3	3	0.4	1.3	1.9	<d.l.	<d.l.	<d.l.	0.9	0.1	0.1	0.1
Sc	INAA (0.01)	9.4	8.26	11.8	11.7	11.8	10.6	8.33	7.18	7.92	17.7	7.4	6.49	1.88	0.86	20.7	8.93	27.2	11.9	7.5	1.9	2.8
Se	INAA (0.5)	<d.l.	<d.l.	<d.l.	<d.l.	<d.l.	<d.l.	<d.l.	<d.l.	<d.l.	<d.l.	<d.l.	<d.l.	<d.l.	<d.l.	<d.l.	<d.l.	<d.l.	0.5	0.5	0.5	0.5
Sn	Fusion-ICP-MS (1)	<d.l.	<d.l.	<d.l.	<d.l.	<d.l.	<d.l.	<d.l.	<d.l.	<d.l.	<d.l.	<d.l.	4	4	4	<d.l.	<d.l.	1	1	1	2	1
Sr	Fusion-ICP (2)	549	449	263	408	615	426	391	271	394	473	214	348	202	34	333	347	350	642	356	40	439
Ta	Fusion-ICP-MS (0.1)	0.7	0.7	0.6	0.6	0.6	0.6	0.7	0.7	0.5	0.4	0.8	2.1	8.1	8.5	0.6	0.7	0.4	0.5	1.1	3.2	1.1
Th	Fusion-ICP-MS (0.05)	7.55	7.95	5.96	9.21	5.88	9.44	7.21	8.06	5.49	4.81	8.98	18.9	70.3	116	6.45	6.73	3.7	5.75	8.88	32.1	14.9
U	Fusion-ICP-MS (0.05)	1.95	1.89	1.56	3.25	3.3	2.33	2.44	1.62	1.55	1.6	2.74	7.89	12.5	8.26	2.19	1.69	1.35	2.19	1.95	7.93	2.69
V	Fusion-ICP (5)	102	84	134	130	131	117	86	67	75	193	63	60	17	<d.l.	154	79	241	188	79	5	33
W	INAA (1)	<d.l.	<d.l.	<d.l.	<d.l.	<d.l.	<d.l.	<d.l.	2	<d.l.	<d.l.	<d.l.	<d.l.	3	<d.l.	<d.l.	<d.l.	<d.l.	2	<d.l.	<d.l.	<d.l.
Y	Fusion-ICP (1)	19	16	17	16	19	17	17	10	12	23	13	22	36	36	22	13	29	19	16	11	12
Zn	MULT INAA/TD-ICP-MS (1)	32	28	32	116	48	34	28	25	29	57	63	24	15	10	62	19	52	37	21	14	20
Zr	Fusion-ICP-MS (1)	125	113	100	148	121	149	152	104	119	127	112	265	381	131	127	106	113	110	132	112	111
La	Fusion-ICP-MS (0.05)	27.1	20.3	21.7	20.1	27.7	25.2	26.4	21.7	22.7	18.4	26.5	40.8	65.6	79.3	16.3	23.7	19.6	25.7	28.4	30.5	32.5
Ce	Fusion-ICP-MS (0.1)	53.2	39.9	41.5	35.6	46.9	43.7	45.8	37.1	39	39.9	47.7	79.5	123	152	32.6	43.1	42	45.5	49	47.3	55.8
Pr	Fusion-ICP-MS (0.02)	5.94	4.51	4.59	4.1	5.29	4.92	5.19	3.72	4.07	4.91	4.91	8.42	11.8	13.4	3.76	4.47	5.28	4.7	4.61	4.52	5.2
Nd	Fusion-ICP-MS (0.05)	22.2	17.4	17.9	13.6	17.2	15.8	16.6	12.7	15.1	20.2	17.4	29.8	38.8	40.2	15	16	21.8	17.1	14.7	11.8	15.2
Sm	Fusion-ICP-MS (0.01)	4.21	3.54	3.48	2.82	3.59	3.26	3.31	2.14	2.85	4.43	3.1	5.37	6.63	7.06	3.45	2.96	4.99	3.79	2.98	1.83	2.73
Eu	Fusion-ICP-MS (0.005)	1.24	1.01	1.06	0.856	1.05	0.979	0.93	0.733	0.974	1.32	0.903	1.22	1.24	0.476	1.31	0.887	1.41	1.17	0.833	0.232	0.694

Table 1 (continued)

Location		Çöpler–Kabataş											Divriği			Yamadağ	Çaltı	Bizmişen	Çöpler–Kabataş	Doğanşehir	Karamadazı	Horoz
Sample no.		C-014	C-104	C-163	C-164	C-166	C-169	C-173	CR-01	CR-02	CR-03	CR-05	CR-07	CR-08	CR-09	CR-10	CR-11	CR-12	CR-14	CR-24	CR-28	CR-31
Lithology[a]		Hbl Diorite Porphyry	Grd. Porphyry	Grd. Porphyry	Grd. Porphyry	Hbl Diorite Porphyry	Grd. Porphyry	Grd. Porphyry	Quartz Diorite	Quartz Diorite	Diorite Porphyry	Quartz Diorite	Quartz Monzonite	Quartz Monzonite	Alk. Feld. Granite	Basaltic Andesite	Tonalite	Diorite	Hbl Diorite Porphyry	Tonalite	Granite	Granite
Alteration		Least-alt.	Least-alt.	Alt. (prop)	Alt. (prop)	Alt. (prop)	Alt. (K)	Least-alt.	Least-alt.	Least-alt.	Least-alt.	Alt. (phyl)	Least-alt.	Least-alt.	Least-alt.	Least-alt.	Least-alt.	Least-alt.	Alt. (prop)	Least-alt.	Least-alt.	Least-alt.
Gd	Fusion-ICP-MS (0.02)	3.5	2.92	2.93	2.88	3.5	3.04	3.05	1.76	2.33	4.05	2.56	4.25	5.11	5.23	3.59	2.31	4.75	3.68	2.67	1.36	2.08
Tb	Fusion-ICP-MS (0.01)	0.59	0.49	0.51	0.49	0.57	0.51	0.52	0.3	0.39	0.71	0.42	0.74	0.98	1.12	0.67	0.41	0.86	0.57	0.45	0.24	0.32
Dy	Fusion-ICP-MS (0.02)	3.45	2.92	3.08	2.63	3.1	2.83	2.86	1.78	2.26	4.39	2.45	4.09	6.08	6.78	4.2	2.46	5.41	3.37	2.76	1.62	1.87
Ho	Fusion-ICP-MS (0.01)	0.69	0.58	0.61	0.53	0.61	0.57	0.57	0.37	0.47	0.88	0.5	0.8	1.23	1.31	0.84	0.49	1.09	0.69	0.58	0.39	0.39
Er	Fusion-ICP-MS (0.01)	2.03	1.79	1.79	1.6	1.83	1.75	1.74	1.18	1.4	2.61	1.54	2.42	4	4.23	2.46	1.48	3.25	2.09	1.8	1.48	1.27
Tl	Fusion-ICP-MS (0.05)	0.25	0.45	0.5	1	0.63	0.63	0.63	0.28	0.86	0.17	0.26	0.64	0.49	0.68	0.29	0.23	0.14	0.48	0.15	1.25	0.28
Tm	Fusion-ICP-MS (0.005)	0.31	0.283	0.27	0.244	0.279	0.261	0.266	0.188	0.224	0.39	0.237	0.373	0.659	0.697	0.364	0.238	0.489	0.31	0.277	0.293	0.203
Yb	Fusion-ICP-MS (0.01)	2.08	1.91	1.8	1.67	1.87	1.74	1.79	1.31	1.54	2.46	1.58	2.4	4.43	4.42	2.33	1.6	3.11	2.02	1.85	2.25	1.43
Lu	Fusion-ICP-MS (0.002)	0.32	0.285	0.282	0.289	0.305	0.29	0.302	0.219	0.24	0.363	0.247	0.367	0.641	0.614	0.355	0.249	0.46	0.32	0.306	0.38	0.241

Element concentrations below the detection limits are indicated as <d.l.

alk feld alkali feldspar, *alt* altered, *grd* granodiorite, *hbl* hornblende, *ICP-MS* inductively coupled plasma mass spectrometry, *INAA* instrumental neutron activation analysis, *K* potassic, *LOI* loss-on-ignition, *MULT* multiple analytical methods, *phyl* phyllic, *prop* propylitic, *TD* total dis

[a] Based on field names

Laboratories in Ontario, Canada. Major and trace element compositions were obtained by a combination of inductively coupled plasma (ICP), inductively coupled plasma emission mass spectrometry (ICP-MS), and instrumental neutron activation analysis (INAA) methods. Replicate analyses of international standards indicate accuracy to within five relative percent for major and minor elements and to within ten relative percent of the standard values for trace elements. Results are listed in Table 1, and major oxide compositions were recalculated to a volatile-free basis totalling 100 wt% for plotting and classification purposes.

$^{40}Ar/^{39}Ar$ geochronology

Mineral separates of biotite, hornblende, and sericite were prepared at the University of Alberta using crushing/sieving and standard heavy liquid and magnetic separation techniques. Individual grains were then hand-picked under a binocular microscope and sent to the Noble Gas Laboratory, Pacific Centre for Isotopic and Geochemical Research, University of British Columbia, Canada, for analysis by T. Ullrich. Samples and flux monitors were wrapped in aluminum foil and sent for irradiation at the McMaster University reactor in Canada. After irradiation, the samples were heated in incremental steps under the defocused beam of a 10 W CO_2 laser (New Wave Research MIR10) until fused. The Ar isotopic composition of the gas emitted from each step was analyzed using a VG5400 mass spectrometer. Isotopic ratios were corrected for total system blank, mass spectrometer sensitivity, mass discrimination, radioactive decay of ^{37}Ar and ^{39}Ar during and subsequent to irradiation, and interfering argon from atmospheric contamination and the irradiation of Ca, Cl, and K.

Re–Os geochronology

Selected quartz–magnetite–sulfide vein samples were pulverized in a porcelain disk mill, and molybdenite was then separated from other sulfide and gangue phases using heavy liquid techniques, magnetic separation, and by flotation using high-purity water. Finally, molybdenite grains were handpicked under a binocular microscope.

The ^{187}Re and ^{187}Os concentrations in molybdenite were determined by isotope dilution mass spectrometry at the University of Alberta Radiogenic Isotope Facility. Dissolution of molybdenite separates and equilibration of sample and tracer Re and Os were done using the Carius tube method (Shirey and Walker 1995).

Samples were dissolved and equilibrated with a "mixed double" spike containing a known amount of ^{185}Re + ^{188}Os + ^{190}Os in 8 ml of reverse aqua regia (3:1, 16 N HNO_3: 12 N HCl) at 220 °C for 48 h. Os and Re were separated by solvent extraction, microdistillation, and anion chromatography techniques (Selby and Creaser 2004). The purified Os and Re fractions were loaded onto Ba-coated Pt or Ni filaments and measured with Faraday collectors using negative thermal ionization mass spectrometry (Creaser et al. 1991; Völkening et al. 1991) on a Micromass Sector 54 mass spectrometer. Total procedure blanks are on the order of <5 pg for Re, and <2 pg for Os.

Errors (2σ) include uncertainties in Re and Os isotopic measurements, Re and Os isotope composition reproducibility of standards, calibration and gravimetric uncertainties of ^{187}Re and ^{187}Os, and uncertainties in the ^{187}Re decay constant. Uncertainties in weights of sample and tracer solution do not affect the calculated age and are not considered.

Whole-rock geochemistry of the Çöpler–Kabataş magmatic complex

The results of whole-rock geochemical analyses are listed in Table 1.

Major elements

Least-altered and altered intrusive and hypabyssal igneous rocks from the Çöpler–Kabataş magmatic complex are plotted on a total alkali versus silica diagram in Fig. 9 (after Middlemost 1994). All least-altered samples from the Çöpler–Kabataş magmatic complex display subalkaline character (medium- to high-K calc-alkaline) and most plot within the granodiorite field, with silica contents ranging from 63.7 to 68.1 wt%. Three samples have lower silica contents (between 56.4 and 58.1 wt% SiO_2), with one least-altered sample (CR-03) and one propylitically altered sample (C-166) plotting within the diorite field, and another propylitically altered sample (CR-14) lying in the monzonite field. The slightly elevated alkali contents of the two propylitically altered samples might be due to sericitization of feldspars and are not thought to reflect primary magma compositions. A compositional gap (between 58 and 64 wt% SiO_2) exists between the fresh diorite porphyry (CR-03) and the rest of the least-altered igneous lithologies from the magmatic complex.

Major and minor oxide compositions of the least-altered magmatic rocks from the Çöpler–Kabataş magmatic complex define roughly linear trends when plotted against SiO_2 on Harker-type diagrams (Fig. 10), suggesting a similar parentage for these rocks. Most major oxides display weak to moderate negative trends with increasing silica content, consistent with fractional crystallization of minerals such as pyroxene, amphibole, and plagioclase, which occur as phenocryst phases. Na_2O, on the other hand, shows a nearly flat trend, whereas K_2O abundance increases slightly with

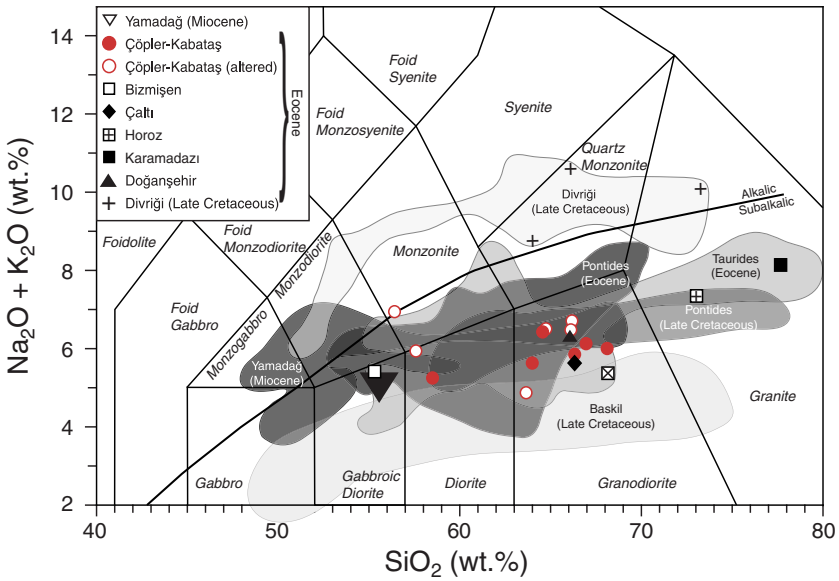

Fig. 9 Total-alkali versus silica diagram (after Middlemost 1994) for least altered and altered intrusive rocks from the Çöpler–Kabataş magmatic complex (data recalculated 100 % volatile-free) plotted together with a suite of regional samples obtained from various Late Cretaceous–Eocene intrusive systems across the central eastern Taurides, and one extrusive rock sample from the Yamadağ volcanic center. Also plotted are the ranges of compositions from the same localities as well as felsic to intermediate compositions from the Eocene Pontide magmatic belt as compiled from previously published data. Data sources: Eocene Tauride intrusions, Gençalioğlu-Kuşcu et al. (2001), Önal et al. (2005), Kadıoğlu and Dilek (2010); Divriği, Boztuğ et al. (2007); Yamadağ volcanic center, Kürüm et al. (2008); Baskil intrusive complex, Rızaoğlu et al. (2009); Pontides, Karslı et al. (2007, 2010a, b). Alkaline–subalkaline boundary from Irvine and Baragar (1971)

increasing silica content until late stages of fractionation (~67 wt% SiO_2).

Trace elements

All samples from the Çöpler–Kabataş magmatic complex have similar trace element compositions, as illustrated on a primitive mantle-normalized trace element diagram (Fig. 11). The samples are enriched in incompatible elements, particularly large ion lithophile elements (LILE) when compared to high field strength elements (HFSE). Positive peaks for Pb and Sb and negative anomalies for Nb, Ta, and Ti are typical of magmas related to subduction (Brenan et al. 1994; Stolz et al. 1996).

Rare earth elements (REE) in Çöpler–Kabataş samples show distinctive listric-shaped patterns on a chondrite-normalized diagram (Fig. 12), with moderate enrichments in light rare earth elements (LREE) relative to middle (MREE) and heavy rare earth elements (HREE), and flat to upward-trending (listric) slopes between MREE and HREE (Fig. 12). This pattern is commonly ascribed to hornblende fractionation or residual hornblende in the source region because hornblende preferentially partitions MREE (Frey et al. 1978; Hanson 1980). The lack of significant europium anomalies is indicative of either oxidizing conditions (Eu^{3+} cannot be incorporated into plagioclase) and/or hydrous conditions (early plagioclase crystallization being suppressed) during evolution of the Çöpler–Kabataş magmas (Hanson 1980; Carmichael and Ghiorso 1990; Moore and Carmichael 1998). The oxidized and hydrous nature of these magmas is further supported by the abundance of hornblende as a phenocryst phase and the widespread presence of magnetite.

$^{40}Ar/^{39}Ar$ geochronology

A summary of the of $^{40}Ar/^{39}Ar$ dating results is presented in Table 2, and apparent age spectra are illustrated in Fig. 13; full analytical data are listed in the Electronic Supplementary Material (ESM 2). Plateau ages are defined using the criteria of Fleck et al. (1977). All samples yielded moderately to well-defined plateaus and calculated plateau ages that are within error of the inverse isochron ages.

Igneous biotite from granodiorite porphyry (C-164), igneous hornblende from hornblende diorite porphyry (C-166), and igneous biotite from quartz diorite (CR-02) from the Çöpler intrusive complex yielded plateau ages of 43.75±0.26 Ma (MSWD=0.20), 44.13±0.38 Ma (MSWD=1.4), and 44.19±0.23 Ma (MSWD=0.49), respectively (Figs. 13a–c). These dates overlap within error and are interpreted to represent cooling ages for these samples.

$^{40}Ar/^{39}Ar$ analysis of hydrothermal alteration minerals associated with mineralization at Çöpler yielded plateau ages close to or overlapping the ages of igneous minerals. Hydrothermal biotite from porphyry-style potassic alteration

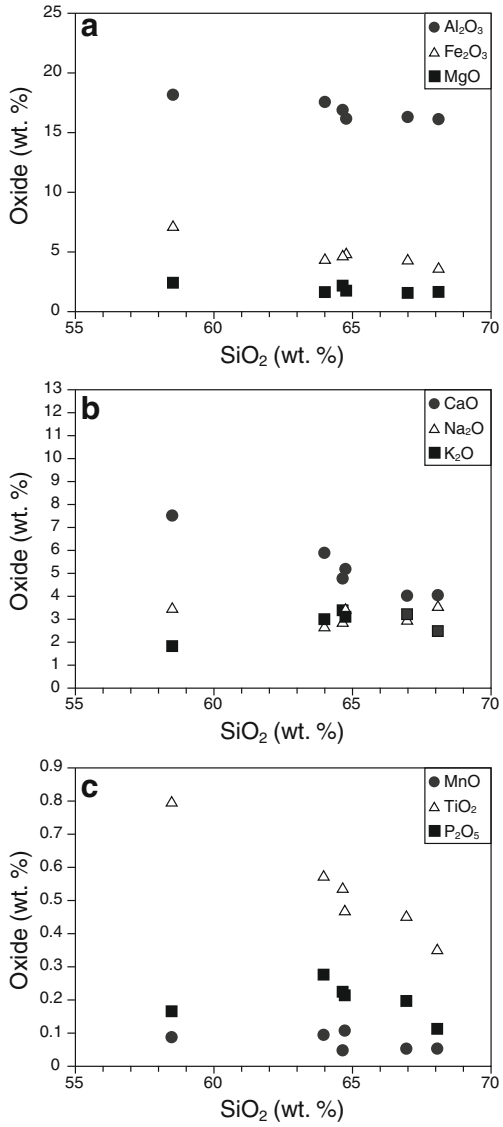

Fig. 10 Harker diagrams showing variation of major and minor oxide abundances relative to SiO_2 for least altered intrusive rocks from the Çöpler–Kabataş magmatic complex

in sample C-169 yielded a plateau age of 43.84±0.26 Ma (MSWD=0.63; Fig. 13d). Sericite from phyllic alteration in sample C-138 yielded a downward stepping spectrum, suggesting the presence of minor excess ^{40}Ar in early steps (Fig. 13e), but the second half of the spectrum includes an acceptable six-step plateau containing more than 50 % of total ^{39}Ar released, with an age of 44.44±0.28 Ma (MSWD=1.05), which should be considered a maximum age. An alternative estimate in samples containing excess ^{40}Ar is provided by the inverse isochron age, which in this case was almost within error of the plateau age at 45.22±0.74 Ma (MSWD=0.23).

Two samples from the Çaltı (CR-11) and Bizmişen (CR-12) intrusions yielded well-defined plateau ages of 44.16±0.23 Ma (MSWD=0.71) and 43.51±0.51 Ma (MSWD=0.76), respectively (Fig. 13f, g), which are similar to the ages from Çöpler. A granite sample (CR-09) from the Divriği area also yielded a well-constrained plateau age of 74.24±0.41 Ma (MSWD=0.18; Fig. 13h), about 30 my older than the Çöpler magmatic system, and consistent with the data previously published by Boztuğ et al. (2007) and Kuşcu et al. (2007).

Re–Os geochronology

Model Re–Os ages were calculated for molybdenite samples C-161 and C-162 from Çöpler, based on the simplified isotope equation: $t=\ln(^{187}Os/^{187}Re+1)/\lambda$, where t is the model age, and λ is the ^{187}Re decay constant ($1.666\times10^{-11}a^{-1}$; Smoliar et al. 1996). The samples yielded ages of 44.6±0.2 and 43.9±0.2 Ma, respectively (Table 3), which are similar to each other, and to the $^{40}Ar/^{39}Ar$ ages of igneous (44.2±0.3 Ma) and hydrothermal (44.4–43.8 Ma) minerals.

Discussion

Interpretation of geochronological data

New geochronological data presented herein constrain the temporal relationship between magmatic and hydrothermal events at the Çöpler–Kabataş magmatic complex. With the exception of two samples, combined $^{40}Ar/^{39}Ar$ and Re–Os ages of igneous and hydrothermal minerals from Çöpler are analytically indistinguishable from each other suggesting rapid cooling conditions within a period of ≤1 my (Fig. 14). This is consistent with the simple intrusive history and the relatively shallow level of emplacement directly beneath the Munzur limestone, which has a maximum thickness of 1,200 m (Özgül and Turşucu 1984; Tunç et al. 1991).

The plateau age of sericite sample obtained from phyllic-altered granodiorite porphyry (44.44±0.28 Ma) and the Re–Os age of one molybdenite-bearing quartz–sulfide vein (44.6±0.2 Ma) are notably older than the $^{40}Ar/^{39}Ar$ plateau age of igneous biotite (43.75±0.26 Ma) obtained from the host granodiorite porphyry (Fig. 14). This discrepancy between the igneous and hydrothermal dates likely suggests thermal resetting of the igneous biotite and hornblende during high temperature potassic alteration, and therefore, at least the younger $^{40}Ar/^{39}Ar$ dates probably represent cooling ages rather than the crystallization age of the Çöpler intrusion. If this is the case, then the older molybdenite age can be explained by the high closure temperature of molybdenite (>700 °C; Bingen and Stein 2003) compared to the Ar diffusion blocking temperature of biotite (250–400 °

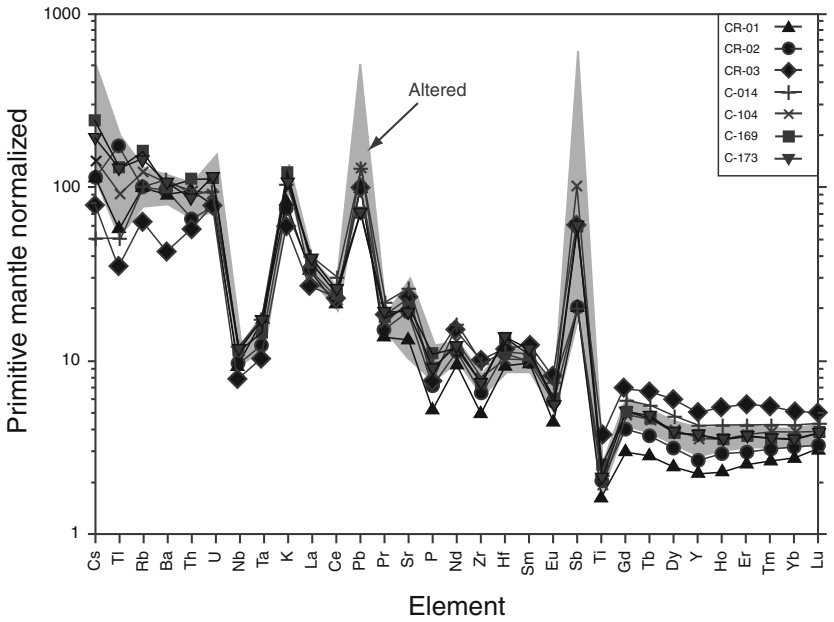

Fig. 11 Primitive mantle-normalized trace element diagram for least altered igneous rocks from the Çöpler–Kabataş magmatic complex. *Gray area* represents altered samples from the region, and the close overlap between least altered and altered samples indicates that hydrothermal alteration has had minimal effect on most trace element compositions in this suite. Normalization values from Sun and McDonough (1989)

C; Richards and Noble 1998) and hornblende (~500 °C). However, based on the close agreement between these cooling ages and the plateau age of igneous biotite (44.19± 0.23 Ma) from unaltered quartz diorite immediately to the east of Çöpler, it can be inferred that the hydrothermal event resetting the Ar isotopic system of igneous biotite and hornblende from Çöpler is only slightly younger than the age of pluton emplacement at the Çöpler–Kabataş magmatic complex. This interpretation is further supported by the $^{40}Ar/^{39}Ar$ dates of igneous biotite and hornblende from the unaltered Çaltı and Bizmişen plutons, which yielded plateau ages of 44.16±0.23 and 43.51± 0.51 Ma, respectively.

Molybdenite samples from two quartz–magnetite–sulfide veins from the Çöpler Main Zone yielded Re–Os ages of 44.6±0.2 and 43.9±0.2 Ma, which do not overlap within error. These different ages may represent discrete pulses of molybdenite mineralization, although there is no field or petrographic evidence to confirm this hypothesis.

The timing of the paragenetically later epithermal-style mineralization, on the other hand, could not be determined due to its poor preservation. Minerals such as adularia or sericite, which may have originally been present, have been destroyed by intense weathering and oxidization of the shallow epithermal levels of the system. However, there is no evidence to suggest that this stage of mineralization was

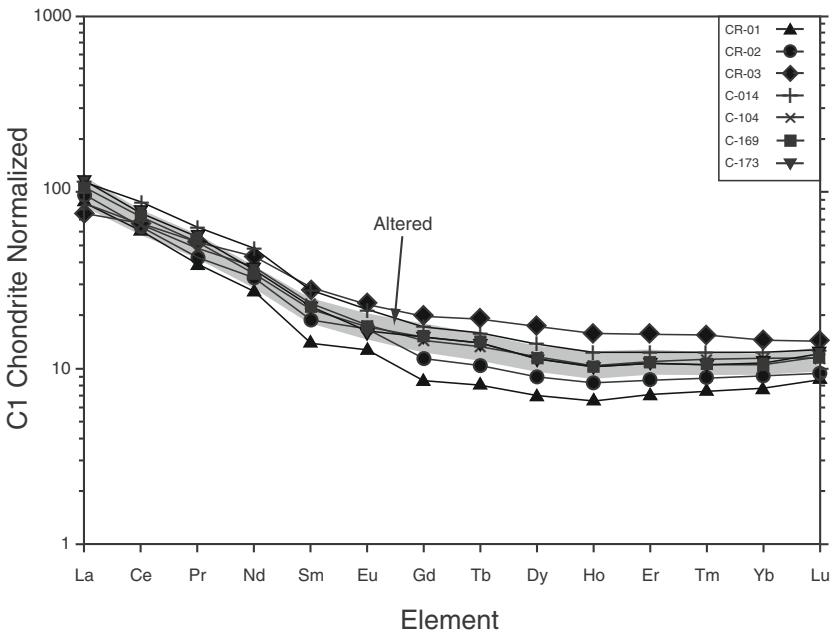

Fig. 12 Chondrite-normalized REE diagram for least altered igneous rocks from the Çöpler–Kabataş magmatic complex. *Gray area* represents altered samples from the region, showing that alteration has not affected rare earth element compositions in these rocks. Normalization values from Sun and McDonough (1989)

Table 2 Summary of $^{40}Ar/^{39}Ar$ dating results from the Çöpler–Kabataş magmatic complex and Bizmişen, Çaltı, and Divriği intrusions

Sample number	Lithology	Mineral	Integrated age±2σ (Ma)	Plateau age±2σ (Ma)	MSWD	Number of steps in plateau/ total steps	% ^{39}Ar released (plateau)	Inverse isochron age±2σ (Ma)	MSWD	Initial $^{40}Ar/^{36}Ar$[a]
Igneous minerals: Çöpler–Kabataş magmatic complex										
C-164	Granodiorite porphyry	Biotite	43.29±0.21	43.75±0.26	0.20	6/9	94	43.70±0.28	0.19	289±24
C-166	Hornblende diorite porphyry	Hornblende	44.43±0.42	44.13±0.38	1.4	8/11	100	43.74±0.49	0.69	307±12
CR-02	Quartz diorite	Biotite	43.97±0.11	44.19±0.23	0.49	11/18	89.5	44.17±0.26	0.65	294±23
Hydrothermal minerals: Çöpler										
C-169	Potassically altered porphyry	Biotite	43.22±0.24	43.84±0.26	0.63	11/17	90.5	43.86±0.30	0.49	292.9±5.1
C-138	Sericitized porphyry	Sericite	44.91±0.16	44.44±0.28	1.05	6/13	53	45.22±0.74	0.23	148±130
Igneous minerals: Çaltı and Bizmişen intrusions										
CR-11	Tonalite	Biotite	44.11±0.11	44.16±0.23	0.71	9/16	77.9	43.68±0.26	1.4	476±36
CR-12	Diorite	Hornblende	42.36±1.11	43.51±0.51	0.76	11/14	98.6	43.40±0.64	0.82	293±2.7
Igneous minerals: Divriği intrusion										
CR-09	Alkali feldspar granite	Biotite	72.89±0.22	74.24±0.41	0.18	7/11	81.3	74.24±0.56	0.21	288±45

[a] Expected $^{40}Ar/^{36}Ar$ composition of atmospheric argon=295.5

Fig. 13 Apparent $^{40}Ar/^{39}Ar$ age spectra for igneous biotite and hornblende from the Çöpler–Kabataş magmatic complex (**a**–**c**), hydrothermal biotite and sericite from the Çöpler porphyry deposit (**d**, **e**), and igneous biotite from nearby central eastern Tauride intrusive centers (**f**–**h**). See Table A1 for sample locations and descriptions. Locations of the samples from the Çöpler deposit are also shown in Fig. 5. Results are summarized in Table 2, and full data are listed in Electronic Supplementary Material (ESM 2)

substantially later than the higher-temperature porphyry-style mineralization.

Petrogenesis of middle Eocene granitoids in the central eastern Taurides

The timing of cooling of the magmatic-hydrothermal system at Çöpler and the inferred crystallization age of the Çöpler–Kabataş magmatic complex (~44 Ma) overlaps with the emplacement ages of the nearby Çaltı (44.16±0.23 Ma) and Bizmişen intrusions (43.51±0.51 Ma) and is slightly younger than the cooling ages of the Horoz, Karamadazı, and Doğanşehir plutons (50–48 Ma; Kuşcu et al. 2007; Karaoğlan et al. 2009) located farther to the southwest. Together, these intrusive centers define a middle Eocene calc-alkaline suite in the central and eastern Taurides, with broadly similar trace element compositions (including enrichments in LREE, negative anomalies of HFSE such as Nb, Ta, Zr, and Ti, and listric-shaped REE patterns; Figs. 15a and 16a). One sample of evolved granite (CR-28) from Horoz shows stronger depletions in Ba, Sr, P, Eu, and Ti, likely due to extensive fractionation of plagioclase, apatite, and Ti-bearing phases (Figs 15a and 16a). In general, however, the geochemical signatures of the middle Eocene granitoids of the central eastern Taurides are consistent with typical arc-related magmatic rocks formed by partial melting of metasomatized mantle wedge above a subducting slab (Brenan et al. 1994; Stolz et al. 1996; Kogiso et al. 1997).

The central eastern Tauride granitoids are currently located approximately 140 km north of the Bitlis Suture, and about 120 km north of the Maden and Helete volcanic belt (Fig. 1), but these distances may have been larger prior to Miocene collision. Thus, these granitoids may have formed in a back-arc environment behind the main Maden and Helete arc and Bitlis subduction zone.

Late Cretaceous–Eocene magmatism along the southeastern TAB margin (Taurides)

The Late Cretaceous (88–70 Ma) Baskil intrusive complex and several granitoid bodies exposed around Göksun–Afşin area represent the earliest stage of arc magmatism along the southern TAB margin. Geochemical data compiled for a range of mafic to felsic subalkaline lithologies (Fig. 9)

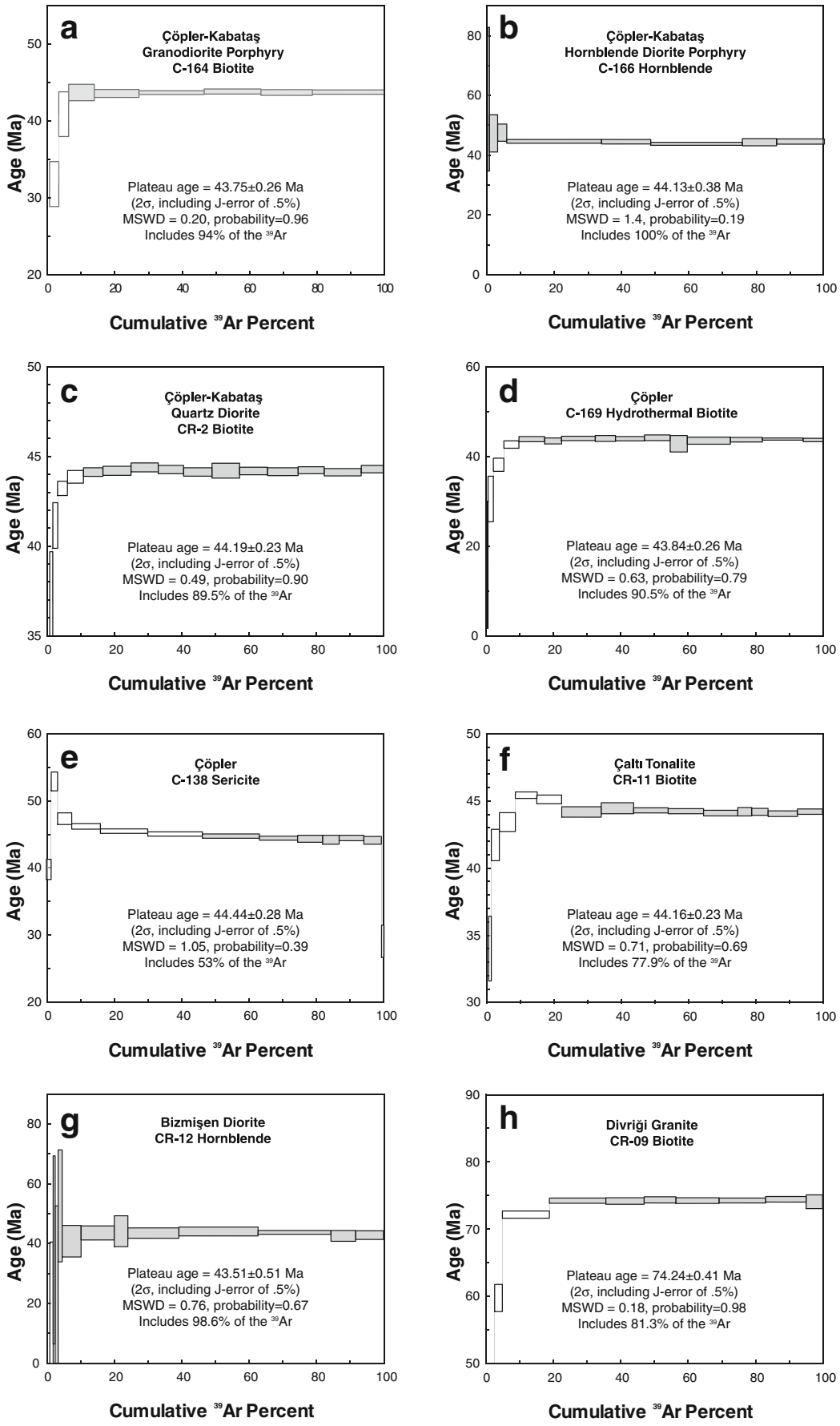
a
Çöpler-Kabataş
Granodiorite Porphyry
C-164 Biotite
Plateau age = 43.75±0.26 Ma
(2σ, including J-error of .5%)
MSWD = 0.20, probability=0.96
Includes 94% of the 39Ar
b
Çöpler-Kabataş
Hornblende Diorite Porphyry
C-166 Hornblende
Plateau age = 44.13±0.38 Ma
(2σ, including J-error of .5%)
MSWD = 1.4, probability=0.19
Includes 100% of the 39Ar
c
Çöpler-Kabataş
Quartz Diorite
CR-2 Biotite
Plateau age = 44.19±0.23 Ma
(2σ, including J-error of .5%)
MSWD = 0.49, probability=0.90
Includes 89.5% of the 39Ar
d
Çöpler
C-169 Hydrothermal Biotite
Plateau age = 43.84±0.26 Ma
(2σ, including J-error of .5%)
MSWD = 0.63, probability=0.79
Includes 90.5% of the 39Ar
e
Çöpler
C-138 Sericite
Plateau age = 44.44±0.28 Ma
(2σ, including J-error of .5%)
MSWD = 1.05, probability=0.39
Includes 53% of the 39Ar
f
Çaltı Tonalite
CR-11 Biotite
Plateau age = 44.16±0.23 Ma
(2σ, including J-error of .5%)
MSWD = 0.71, probability=0.69
Includes 77.9% of the 39Ar
g
Bizmişen Diorite
CR-12 Hornblende
Plateau age = 43.51±0.51 Ma
(2σ, including J-error of .5%)
MSWD = 0.76, probability=0.67
Includes 98.6% of the 39Ar
h
Divriği Granite
CR-09 Biotite
Plateau age = 74.24±0.41 Ma
(2σ, including J-error of .5%)
MSWD = 0.18, probability=0.98
Includes 81.3% of the 39Ar
Age (Ma)
Cumulative 39Ar Percent

Table 3 Summary of Re–Os molybdenite data from the Çöpler deposit

Sample number	Sample location	Drill hole: depth	Re (ppm)	^{187}Re (ppm)	^{187}Os (ppb)	Model age (Ma)	Age uncertainty (±2σ) with decay constant uncertainty (Ma)
C-161	0458723E 4363842N	–	7,031	4,419	3,284	44.6	0.2
C-162	0458802E 4363880N	CDD-140: 180.0–180.1 m	2,242	1,409	1,031	43.9	0.2

indicate relatively unenriched compositions compared to the Çöpler–Kabataş suite (Fig. 15b and 16b), consistent with a continental arc origin for these granitoids (Yazgan and Chessex 1991; Parlak 2006; Rızaoğlu et al. 2009).

After a period of quiescence in the Paleocene, magmatism along the southern TAB margin resumed in the middle Eocene with eruption of the Maden and Helete volcanic rocks (Fig. 1). These basaltic to rhyolitic rocks have subalkaline to mildly alkaline character, with enrichments in LILE relative to HFSE, and negative Nb and Zr anomalies (Aktaş and Robertson 1984; Yiğitbaş and Yılmaz 1996a; Elmas and Yılmaz 2003; Robertson et al. 2007). The Helete and Maden suites appear to represent the locus of middle Eocene volcanism above the southern Neotethys subduction zone (Yiğitbaş and Yılmaz 1996a; Robertson et al. 2007).

In comparison, as noted above, the broadly coeval Çöpler–Kabataş magmatic complex, located 120 km further north, likely represents a back arc magmatic system. A similar tectonomagmatic setting may also be invoked for Eocene magmatism along the transtensional Göksu–Yazyurdu and Malatya–Ovacık fault zones. Paleocene–Eocene slab rollback beneath southeast Anatolia (Robertson et al. 2007; Kaymakçı et al. 2010) may have caused extension in the overriding plate, and subsequent initiation of these back-arc systems, and may also be responsible for the anomalous curvatures of the Bitlis sector of the southern Neotethyan subduction zone and the adjacent Cypriot arc to the southwest (Fig. 2c; Schellart and Lister 2004; Wallace et al. 2009). Similar middle Eocene back-arc magmatism occurred behind the main axis of the Urumieh–Dokhtar arc in Iran (the eastern continuation of the Maden–Helete arc), producing large volumes of calc-alkaline volcanic and plutonic rocks with subduction signatures (LILE-enriched, HFSE-depleted, and LREE-enriched trace element patterns; Ahmadian et al. 2009; Allen 2009; Verdel et al. 2011; Vincent et al. 2005).

On the other hand, Kuşcu et al. (2010) argued that the middle Eocene volcanism at Maden and Helete, and the Eocene central eastern Tauride granitoids were generated in a postcollisional setting, following the termination of Late Cretaceous subduction magmatism in southeast Anatolia. According to this model, incipient rupturing of the steepened slab led to invasion of hot asthenospheric material beneath the southern TAB margin, which caused the delayed partial melting of subduction-modified mantle sources and subsequent subalkaline to mildly alkaline magmatism in the eastern TAB. However, a problem with this model is that it infers a pre-Eocene timing for the Eurasia–Arabia collision, which is not supported by recent tectonic reconstructions that suggest Miocene collision (e.g., Dewey et al. 1986; McQuarrie et al. 2003; Hüsing et al. 2009; Okay et al. 2010).

Middle Miocene postcollisional magmatism in the TAB

Postcollisional magmatism along the southern TAB margin began during the middle Miocene with eruption of large volumes of subalkaline to mildly alkaline mafic to felsic

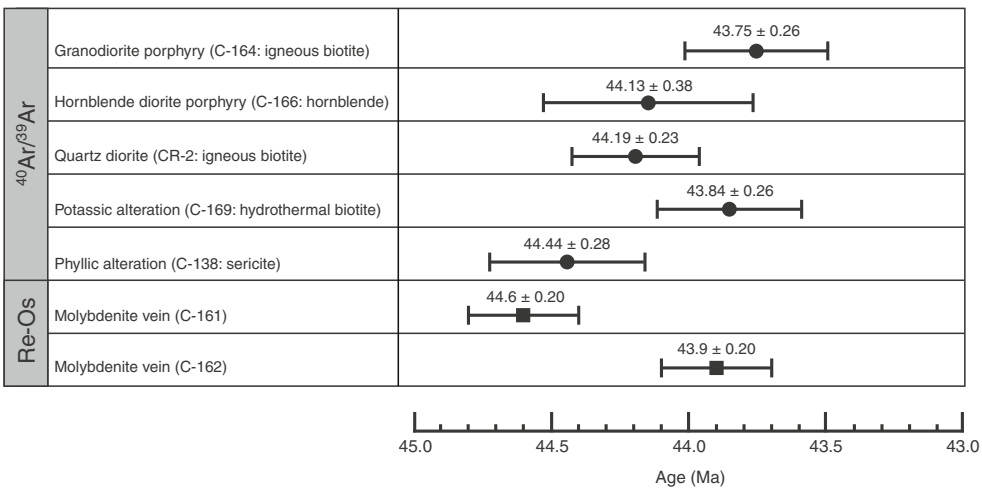

Fig. 14 Summary of ^{40}Ar/^{39}Ar and Re–Os geochronology results for the Çöpler–Kabataş magmatic complex and the Çöpler gold deposit. ^{40}Ar/^{39}Ar dates are plateau ages and Re–Os dates are model ages. Error bars are reported at 2σ

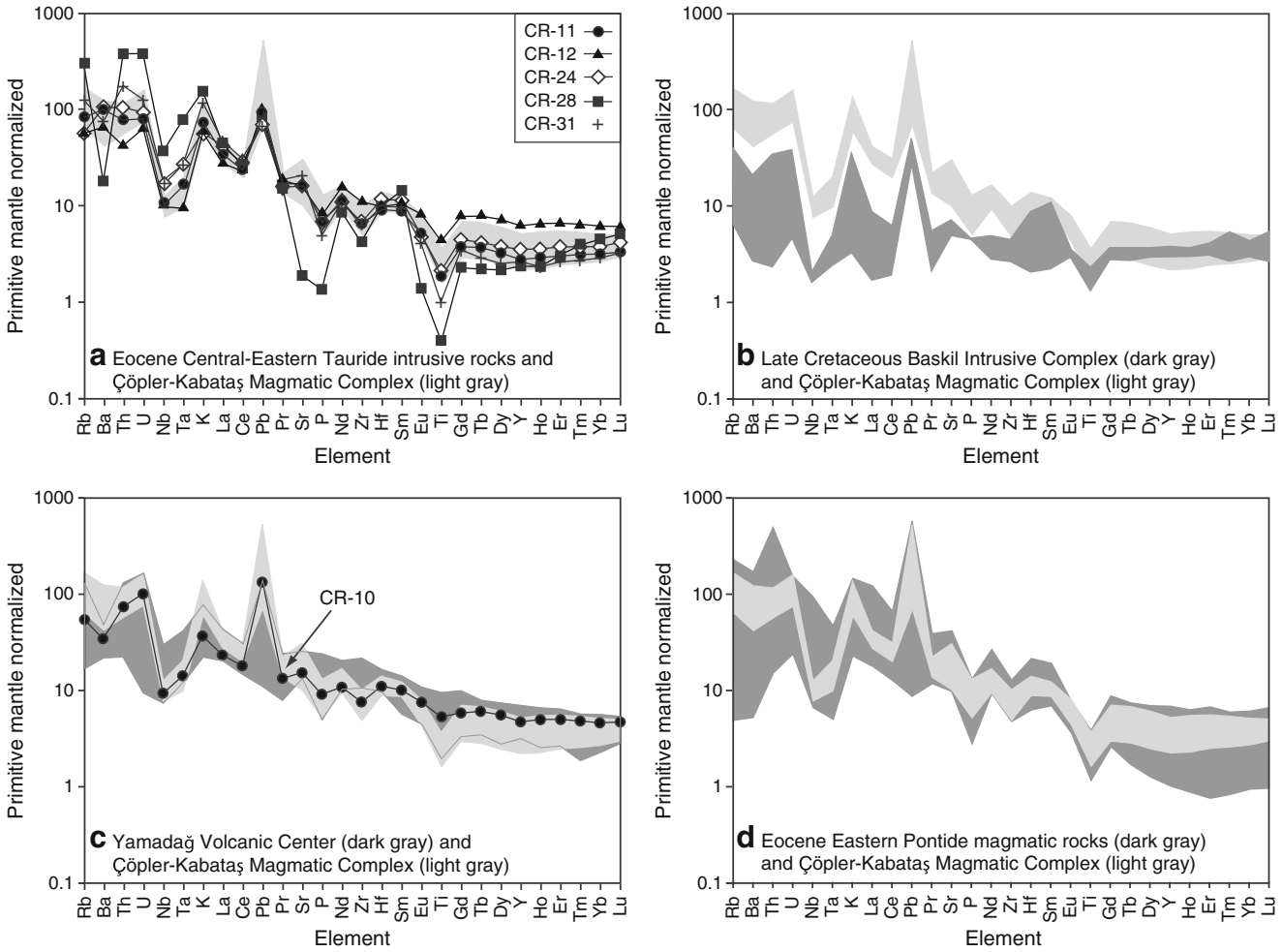

Fig. 15 Primitive mantle-normalized trace element diagrams, showing compositions of **a** Eocene central eastern Tauride plutonic rocks, **b** the Late Cretaceous Baskil intrusive complex, **c** the Miocene Yamadağ volcanic center, and **d** the middle Eocene eastern Pontide plutonic and volcanic rocks, compared with the range of compositions of igneous rocks from the Çöpler–Kabataş magmatic complex (light grey field). Data sources: Baskil intrusive complex: Rızaoğlu et al. (2009); Yamadağ volcanic center: Kürüm et al. (2008). Normalization values from Sun and McDonough (1989)

volcanic rocks, including the Yamadağ volcanic center. Overall, the trace element and REE profiles of the erupted magmas are broadly similar to those of middle Eocene central eastern Tauride intrusions (Figs. 15c and 16c), suggesting derivation from a remnant subduction-modified mantle source beneath the TAB. Partial melting was possibly triggered by slab break-off following early Miocene collision (Keskin 2003; Şengör et al. 2003; Faccenna et al. 2006) or by delamination of the subcontinental lithospheric mantle beneath eastern Anatolia (Pearce et al. 1990; Göğüş and Pysklywec 2008).

Comparison with Eocene magmatism along the northern TAB margin (Pontides)

Middle Eocene (52–41 Ma) plutonic and volcanic sequences also occur along the northern TAB margin in the eastern Pontides and are interpreted to represent postcollisional magmatism following closure of the İzmir–Ankara–Erzincan Ocean (Okay and Şahintürk 1997). These rocks are geochemically quite similar to the Çöpler–Kabataş magmatic rocks (Figs. 9, 15d, and 16d) but, in this case, are indisputably postcollisional. This illustrates the problem of using lithogeochemistry alone as an indicator of tectonic setting because geochemically similar magmas can be generated in back-arc and postsubduction settings.

Metallogenic Implications

The calc-alkaline Çöpler–Kabataş magmatic complex is argued above to have formed in a back-arc setting during the final stages of regional transtension prior to collision, and its location was controlled by a major ENE-trending sinistral fault system.

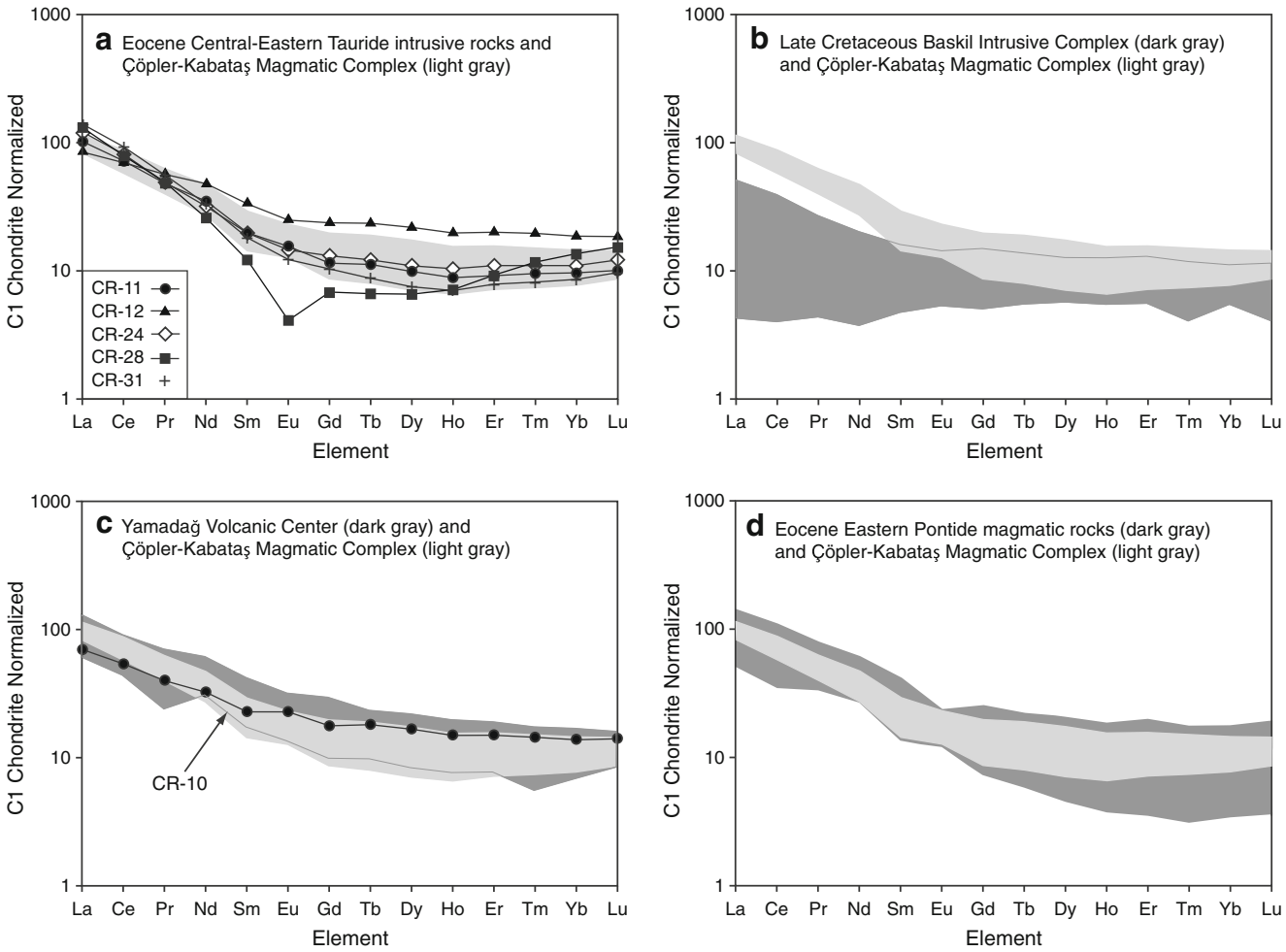

Fig. 16 Chondrite-normalized rare earth element diagrams, showing compositions of **a** Eocene central eastern Tauride plutonic rocks, **b** the Late Cretaceous Baskil intrusive complex, **c** the Miocene Yamadağ volcanic center, **d** the middle Eocene eastern Pontide plutonic and volcanic rocks, compared with the range of compositions of igneous rocks from the Çöpler–Kabataş magmatic complex (*light gray field*). Data sources: Baskil intrusive complex, Rızaoğlu et al. (2009); Yamadağ volcanic center (*light gray field*), Kürüm et al. (2008). Normalization values from Sun and McDonough (1989)

Unlike many porphyry systems that occur as clusters within orogen-parallel volcano-plutonic belts in convergent margin settings, the Çöpler Au–(Cu) deposit is positioned inland from the coeval Maden–Helete arc system. In this respect, Çöpler may have formed in a manner comparable to some other isolated Au-rich porphyry deposits such as the Bajo de la Alumbrera porphyry Cu–Au deposit in northwest Argentina and Bingham Canyon porphyry Cu–Au–Mo deposit in western USA.

The Miocene Farallòn Negro Complex and associated Bajo de la Alumbrera porphyry Cu–Au deposit in Argentina lies about 200 km inland from the main axis of the Andean volcanic arc and is thought to have formed during a period of flattening of subduction, with magmatism being localized by extensional structural intersections in the upper plate (Sasso and Clark 1998; Chernicoff et al. 2002; Halter et al. 2004).

Similarly, the Bingham porphyry Cu–Au–Mo deposit is located far inland with respect to the coeval subduction zone and is proposed to have formed during a period of incipient extension related to steepening/roll-back of the Farallon Plate during the Paleocene (Ryskamp et al. 2008; Sillitoe 2008; Pettke et al. 2010). Pettke et al. (2010) further suggested that the parental magma at Bingham and its ore components were derived from a Proterozoic subduction-modified lithospheric mantle source, which was remelted during the Eocene tectonic activity.

In comparison, collision-related deposits such as Grasberg (Indonesia) and Ok Tedi (Papua New Guinea) are thought to have formed by remelting of subduction-modified lithospheric sources following delamination of the subcontinental lithospheric mantle (McDowell et al. 1996; Cloos et al. 2005; van Dongen et al. 2010). The similarity of magma compositions and deposit styles

between these collision-related and back-arc deposits such as Çöpler suggests that there may be a continuum in terms of tectonomagmatic and metallogenic processes in these broadly subduction-related settings (Richards 2009, 2011).

Conclusions

The Çöpler porphyry-epithermal Au–(Cu) deposit is spatially related to middle Eocene calc-alkaline diorite and granodiorite porphyry stocks, which are interpreted to have formed in a back-arc setting behind the southern Neotethys subduction zone, shortly prior to continent–continent collision in the Miocene. Emplacement of these and other middle Eocene intrusions in the central eastern Taurides was controlled by regionally extensive, ENE-striking, strike-slip fault systems.

$^{40}Ar/^{39}Ar$ ages of igneous minerals from intrusive rocks in the Çöpler–Kabataş magmatic complex range between 44.13±0.38 and 43.75±0.26 Ma, whereas hydrothermal biotite and sericite associated with porphyry-style hydrothermal alteration at Çöpler yielded $^{40}Ar/^{39}Ar$ ages of 43.84±0.26 Ma and 44.44±0.2, respectively. The ~0.7 my range in these ages likely reflects differential cooling in different parts of the magmatic-hydrothermal system and the different closure temperatures to argon diffusion of biotite and sericite. Nevertheless, these cooling ages closely overlap with the age of porphyry-type mineralization obtained from two molybdenite samples (44.6±0.2 and 43.9±0.2 Ma), indicating a short life span for the magmatic-hydrothermal system of ≤1 my, which is consistent with the relatively simple history and shallow emplacement of the intrusive system and ore deposit.

These ages are also similar to the $^{40}Ar/^{39}Ar$ plateau ages of igneous biotite from an unaltered quartz diorite to the east of Çöpler (44.19±0.26 Ma) and igneous biotite and hornblende from the unaltered Çaltı (44.16±0.23 Ma) and Bizmişen (43.51±0.51 Ma) intrusions, indicating that the hydrothermal system at Çöpler developed concurrently with the ~44 Ma back-arc magmatic activity that took place in the eastern Taurides.

The back-arc setting of the Çöpler Au–(Cu) deposit can be compared to other similar porphyry Cu–Au deposits in back-arc or collisional settings, such as Bingham Canyon (USA), Bajo de la Alumbrera (Argentina), and possibly Ok Tedi (Papua New Guinea) and Grasberg (Indonesia).

Acknowledgments This work was funded by a Discovery Grant from the Natural Sciences and Engineering Research Council of Canada (NSERC) to JPR. Partial financial support was provided by the Society of Economic Geologists through a Student Research Grant to Aİ. Logistical support for fieldwork was provided by Anatolia Minerals Development Ltd. (AMDL), and special thanks are due to Firuz Alizade and İlhan Poyraz of the Ankara office for access to the mine site. Ali Ekber Özden, Aşkın Sarpay, and İbrahim Güney of AMDL are thanked for their assistance during fieldwork in 2006, and Orhan Karaman is thanked for his help during collection of regional samples in 2008. We thank Tom Ullrich of the Pacific Centre for Isotopic and Geochemical Research (PCIGR) Noble Gas Laboratory at the University of British Columbia for providing $^{40}Ar/^{39}Ar$ isotopic data. We also thank Sergei Matveev, Mark Labbe, Don Resultay, and everyone at the Radiogenic Isotope Facility at the University of Alberta for their help in sample preparation, and data collection. We thank Thomas Bissig, Kalin Kouzmanov, and Aleksandar Miskovich for their constructive reviews, which helped improve the manuscript.

References

Ahmadian J, Haschke M, McDonald I, Regelous M, RezaGhorbani M, Emami MH, Murata M (2009) High magmatic flux during Alpine–Himalayan collision: constraints from the Kal-e-Kafi complex, central Iran. Geol Soc Am Bull 12:857–868

Aktaş G, Robertson AHF (1984) The Maden Complex, SE Turkey: evolution of a Neotethyan active margin. In: Dixon JE, Robertson AHF (eds) The geological evolution of the Eastern Mediterranean. Geol Soc Lond Spec Publ 17:375–402

Allen MB (2009) Discussion on the Eocene bimodal Piranshahr massif of the Sanadaj-Sirjan Zone, West Iran: a marker of the end of collision in the Zagros orogen. J Geol Soc Lond 166:981–982

Arger J, Mitchell J, Westaway RWC (2000) Neogene and Quaternary volcanism of southeastern Turkey. In: Bozkurt E, Winchester JA, Piper JDA (eds) Tectonics and magmatism in Turkey and surrounding area. Geol Soc Lond Spec Publ 173:1–23

Barley ME, Rak P, Wyman D (2002) Tectonic controls on magmatic-hydrothermal gold mineralization in the magmatic arcs of SE Asia. In: Blundell DJ, Neubauer F, Von Quadt A (eds) The timing and location of major ore deposits in an evolving orogen. Geol Soc Lond Spec Publ 204:39–47

Bierlein FP, Groves DI, Cawood PA (2009) Metallogeny of accretionary orogens—the connection between lithospheric processes and metal endowment. Ore Geol Rev 36:282–292

Bingen B, Stein H (2003) Molybdenite Re–Os dating of biotite dehydration melting in the Rogaland high-temperature granulites, S Norway. Earth Planet Sci Lett 208:181–195

Bozkurt E (2001) Neotectonics of Turkey—a synthesis. Geod Acta 14:3–30

Boztuğ D, Harlavan Y, Arehart GB, Satır M, Avcı N (2007) K-Ar age, whole-rock and isotope geochemistry of A-type granitoids in the Divriği-Sivas region, eastern-central Anatolia, Turkey. Lithos 97:193–218

Brenan JM, Shaw HF, Phinney DL, Ryerson FJ (1994) Rutile-aqueous fluid partitioning of Nb, Ta, Hf, Zr, U and Th: implications for high field strength element depletions in island-arc basalts. Earth Planet Sci Lett 128:327–339

Carmichael ISE, Ghiorso MS (1990) The effect of oxygen fugacity on the redox state of natural liquids and their crystallizing phases. In: Nicholls J, Russell JK (eds), Modern methods of igneous petrology: understanding magmatic processes. Rev Mineral, Min Soc America 24:191–212

Cater JML, Hanna SS, Ries AC, Turner P (1991) Tertiary evolution of the Sivas Basin, central Turkey. Tectonophysics 195:29–46

Chernicoff CJ, Richards JP, Zappettini EO (2002) Crustal lineament control on magmatism and mineralization in northwestern Argentina: geological, geophysical, and remote sensing evidence. Ore Geology Reviews 21:127–155

Cloos M, Sapiie B, van Ufford AQ, Weiland RJ, Warren PQ McMahon TP (2005) Collisional delamination in New Guinea: the geotectonics of subducting slab breakoff. Geol Soc Am Spec Pap 400, p. 51

Creaser RA, Papanastassiou DA, Wasserburg GJ (1991) Negative thermal ion mass spectrometry of osmium, rhenium and iridium. Geochim Cosmochim Acta 55:397–401

Dewey JF, Hempton MR, Kidd WSF, Şaroğlu F, Şengör AMC (1986) Shortening of continental lithosphere: the neotectonics of Eastern Anatolia—a young collision zone. In: Coward MP, Ries AC (eds) Collision tectonics. Geol Soc Lond Spec Publ 19:3–36

Dewey JF, Helman ML, Turco E, Hutton DWH, Knott SD (1989) Kinematics of the western Mediterranean. In: Coward MP, Dietrich D, Park RG (eds) Alpine tectonics. Geol Soc Lond Spec Publ 45:265–283

Ekici T, Alpaslan M, Parlak O, Uçurum A (2009) Geochemistry of the middle Miocene collision-related Yamadağı (eastern Anatolia) calc-alkaline volcanics, Turkey. Turk J Earth Sci 18:511–528

Elmas A, Yılmaz Y (2003) Development of an oblique subduction zone—tectonic evolution of the Tethys suture zone in southeast Turkey. Int Geol Rev 45:827–840

Faccenna C, Bellier O, Martinod J, Piromallo C, Regard V (2006) Slab detachment beneath eastern Anatolia: a possible cause for the formation of the North Anatolian fault. Earth Planet Sci Lett 242:85–97

Fayon AK, Whitney DL, Teyssier C, Garver JI, Dilek Y (2001) Effects of plate convergence obliquity on timing and mechanisms of exhumation of a mid-crustal terrain, the Central Anatolian Crystalline Complex. Earth Planet Sci Lett 192:191–205

Fleck RJ, Sutter JF, Elliot DH (1977) Interpretation of discordant $^{40}Ar/^{39}Ar$ age-spectra of Mesozoic tholeiites from Antarctica. Geochim Cosmochim Acta 41:15–32

Frey FA, Chappell BW, Roy SD (1978) Fractionation of rare-earth elements in the Tuolumne intrusive series, Sierra Nevada batholith, California. Geology 6:239–242

Gautier P, Bozkurt E, Hallot E, Dirik K (2002) Dating the exhumation of a metamorphic dome: geological evidence for pre-Eocene unroofing of the Niğde Massif (Central Anatolia, Turkey). Geol Mag 139:559–576

Gençalioğlu-Kuşcu G, Göncüoğlu MC, Kuşcu İ (2001) Post-collisional magmatism on the northern margin of the Taurides and its geological implications: geology and petrology of the Yahyalı-Karamadazı Granitoid. Turk J Earth Sci 10:103–119

Glazner AF (1991) Plutonism, oblique subduction, and continental growth: an example from the Mesozoic of California. Geology 19:784–786

Göğüş OH, Pysklywec RN (2008) Mantle lithosphere delamination driving plateau uplift and synconvergent extension in eastern Anatolia. Geology 36:723–726

Halter WE, Bain N, Becker K, Heinrich CA, Landtwing M, VonQuadt A, Clark AH, Sasso AM, Bissig T, Tosdal RM (2004) From andesitic volcanism to the formation of a porphyry Cu–Au mineralizing magma chamber: the Farallòn Negro Volcanic Complex, northwestern Argentina. J Volcanol Geotherm Res 136:1–30

Hanson GN (1980) Rare earth elements in petrogenetic studies of igneous systems. Annu Rev Earth Planetary Sci 8:371–406

Hedenquist JW, Lowenstern JB (1994) The role of magmas in the formation of hydrothermal ore deposits. Nature 370:519–527

Hou Z, Cook NJ (2009) Metallogenesis of the Tibetan collisional orogen: a review and introduction to the special issue. Ore Geol Rev 36:2–24

Hüsing SK, Zachariasse W-J, van Hinsbergen DJJ, Krijgsman W, İnceöz M, Harzhauser M, Mandic O, Kroh A (2009) Oligocene–Miocene basin evolution in SE Anatolia, Turkey: constraints on the closure of the eastern Tethys gateway. In: van Hinsbergen DJJ, Edwards MA, Gowers R (eds) Collision and collapse at the Africa–Arabia–Eurasia subduction Zone. Geol Soc Lond Spec Publ 311:107–132

Hutton DHW (1982) A tectonic model for the emplacement of the Main Donegal Granite, NW Ireland. J Geol Soc Lond 139:615–631

Hutton DHW, Dempster TJ, Brown PE, Becker SD (1990) A new mechanism of granite emplacement: intrusion in active extensional shear zones. Nature 343:452–455

Irvine TN, Baragar WRA (1971) A guide to the chemical classification of the common volcanic rocks. Can J Earth Sci 8:523–548

Janković S (1977) The copper deposits and geotectonic setting of the Tethyan Eurasian Metallogenic Belt. Miner Deposita 12:37–47

Kadıoğlu YK, Dilek Y (2010) Structure and geochemistry of the adakitic Horoz granitoid, Bolkar Mountains, south-central Turkey, and its tectonomagmatic evolution. Int Geol Rev 52:505–535

Kadıoğlu YK, Dilek Y, Foland KA (2006) Slab breakoff and syncollisional origin of the Late Cretaceous magmatism in the Central Anatolian Crystalline Complex, Turkey. In: Dilek Y, Pavlides S (eds) Postcollisional tectonics and magmatism in the Mediterranean region and Asia. Geol Soc Am Spec Pap 409:381–415

Karaoğlan F, Parlak O (2006) Geochemistry and tectonic significance of the Doğanşehir (Malatya) granitoid. Abstracts of the 59th Geological Congress of Turkey, Ankara, 20–24 March 2006, pp 495–496.

Karaoğlan F, Parlak O, Kloetzli U, Thöni M, Koller F, Hejl E, Rızaoğlu T (2009) Geochronology and isotope geochemistry of the ophiolites and granitoids along the southeast Anatolian orogenic belt. Abstracts of the 62nd Geological Congress of Turkey, Ankara, 13–17 April 2009, pp. 846–847.

Karslı O, Chen B, Aydın F, Şen C (2007) Geochemical and Sr–Nd–Pb isotopic compositions of the Eocene Dölek and Sarıçiçek Plutons, Eastern Turkey: implications for magma interaction in the genesis of high-K calc-alkaline granitoids in a post-collision extensional setting. Lithos 98:67–96

Karslı O, Dokuz A, Uysal İ, Aydın F, Chen B, Kandemir R, Wijbrans J (2010a) Relative contributions of crust and mantle to generation of Campanian high-K calc-alkaline I-type granitoids in a subduction setting, with special reference to Harşit Pluton, eastern Turkey. Contrib Mineral Petrol 160:467–487

Karslı O, Dokuz A, Uysal İ, Aydın F, Kandemir R, Wijbrans J (2010b) Generation of the Early Cenozoic adakitic volcanism by partial melting of mafic lower crust, Eastern Turkey: implications for crustal thickening to delamination. Lithos 114:109–120

Kaymakçı N, White SH, Van Dijk PM (2000) Palaeostress inversion in a multiphase deformed area: kinematic and structural evolution of the Çankırı Basin (central Turkey), Part 1—northern area. In: Bozkurt E, Winchester JA, Piper JDA (eds) Tectonics and magmatism in Turkey and surrounding area. Geol Soc Lond Spec Publ 173:295–323

Kaymakçı N, İnceöz M, Ertepınar P (2006) 3D-architecture and Neogene evolution of the Malatya Basin: inferences for the Kinematics of the Malatya and Ovacık Fault Zones. Turk J Earth Sci 15:123–154

Kaymakçı N, İnceöz M, Ertepınar P, Koç A (2010) Late Cretaceous to recent kinematics of SE Anatolia (Turkey). In: Sosson M, Kaymakçı N, Stephenson RA, Bergerat F, Starostenko V (eds) Sedimentary basin tectonics from the Black Sea and Caucasus to the Arabian Platform. Geol Soc Lond Spec Publ 340:409–435.

Keskin M (2003) Magma generation by slab steepening and breakoff beneath a subduction-accretion complex: an alternative model for collision-related volcanism in Eastern Anatolia. Turkey Geophys Res Lett 30:8046. doi:10.1029/2003GL018019

Keskin M, Genç ŞC, Tüysüz O (2008) Petrology and geochemistry of post-collisional Middle Eocene volcanic units in North-Central Turkey: evidence for magma generation by slab breakoff following the closure of the Northern Neotethys Ocean. Lithos 104:267–305

Kesler SE (1997) Metallogenic evolution of convergent margins: selected ore deposit models. Ore Geol Rev 12:153–171

Koçyiğit A, Beyhan A (1998) A new intracontinental transcurrent structure: the Central Anatolian Fault Zone, Turkey. Tectonophysics 284:317–336

Kogiso T, Tatsumi Y, Nakano S (1997) Trace element transport during dehydration processes in the subducted crust: 1. Experiments and implications for the origin of ocean island basalts. Earth Planet Sci Lett 148:193–205

Kürüm S, Önal A, Boztuğ D, Spell T, Arslan M (2008) $^{40}Ar/^{39}Ar$ age and geochemistry of the post-collisional Miocene Yamadağ volcanics in the Arapkir area (Malatya Province), eastern Anatolia, Turkey. J Asian Earth Sci 33:229–251

Kuşcu İ, Gençalioğlu-Kuşcu G, Tosdal RM (2007) Tectonomagmatic-metallogenic framework of mineralization events in the southern NeoTethyan arc, southeastern Turkey. In: Andrew CJ et al (eds) Digging Deeper. Proceedings of the 9th Biennial SGA Meeting, Dublin, 20–23 August 2007, pp. 853–856.

Kuşcu İ, Gençalioğlu-Kuşcu G, Tosdal RM, Ulrich TD, Friedman R (2010) Magmatism in the southeastern Anatolian orogenic belt: transition from arc to post-collisional setting in an evolving orogen. In: Sosson M, Kaymakçı N, Stephenson RA, Bergerat F, Starostenko V (eds) Sedimentary basin tectonics from the Black Sea and Caucasus to the Arabian Platform. Geol Soc Lond Spec Publ 340:437–460

Lei J, Zhao D (2007) Teleseismic evidence for a break-off subducting slab under Eastern Turkey. Earth Planet Sci Lett 257:14–28

Marschik R, Spikings R, Kuşcu İ (2008) Geochronology and stable isotope signature of alteration related to hydrothermal magnetite ores in Central Anatolia, Turkey. Miner Deposita 43:111–124

McDowell FW, McMahon TP, Warren PQ, Cloos M (1996) Pliocene Cu–Au bearing intrusions of the Gunung Bijih (Ertsberg) district, Irian Jaya, Indonesia: K-Ar geochronology. J Geol 104:327–340

McKenzie D, Yılmaz Y (1991) Deformation and volcanism in western Turkey and the Aegean. Bull Tech Univ İstanbul 44:345–373

McQuarrie N, Stock JM, Verdel C, Wernicke B (2003) Cenozoic evolution of Neotethys and implications for the causes of plate motions. Geophys Res Lett 30:2036. doi:10.1029/2003GL017992

Michard A, Whitechurch H, Ricou LE, Montigny R, Yazgan E (1984) Tauric subduction (Malatya-Elazığ provinces) and its bearing on tectonics of the Tethyan realm in Turkey. In: Dixon JE, Robertson AHF (eds) The geological evolution of the Eastern Mediterranean. Geol Soc Lond Spec Publ 17:361–373

Middlemost EAK (1994) Naming materials in the magma/igneous rock system. Earth Sci Rev 37:215–224

Moore G, Carmichael ISE (1998) The hydrous phase equilibria (to 3 kbar) of an andesite and basaltic andesite from western Mexico: Constraints on water content and conditions of phenocryst growth. Contrib Mineral Petrol 130:304–319

MTA (1989) Geologic map of Turkey. Ankara, MTA, scale 1:2,000,000

MTA (2002a) Geologic map of Turkey (Sivas Quadrangle). Ankara, MTA, scale 1:500,000

MTA (2002b) Geologic map of Turkey (Erzurum Quadrangle). Ankara, MTA, scale 1:500,000

Okay Aİ, Şahintürk O (1997) Geology of the eastern Pontides. In: Robinson AG (ed) Regional and petroleum geology of the Black Sea and surrounding region. Am Assoc Petrol Geol Mem 68:291–311

Okay Aİ, Tüysüz O (1999) Tethyan sutures of northern Turkey. In: Durand B, Jolivet L, Horvath F, Seranne M (eds) Mediterranean basins: tertiary extension within the Alpine Orogen. Geol Soc Lond Spec Publ 156:475–515

Okay Aİ, Tansel İ, Tüysüz O (2001) Obduction, subduction and collision as reflected in the Upper Cretaceous–Lower Eocene sedimentary record of western Turkey. Geol Mag 138:117–142

Okay Aİ, Satır M, Siebel W (2006) Pre-Alpide Palaeozoic and Mesozoic orogenic events in the Eastern Mediterranean region. In: Gee DG, Stephenson RA (eds) European lithosphere dynamics. Geol Soc Lond Mem 32:389–405

Okay Aİ, Zattin M, Cavazza W (2010) Apatite fission-track data for the Miocene Arabia–Eurasia collision. Geology 38:35–38

Önal A, Boztuğ D, Kürüm S, Harlavan Y, Arehart GB, Arslan M (2005) K-Ar age determination, whole-rock and oxygen isotope geochemistry of the post-collisional Bizmişen and Çaltı plutons, SW Erzincan, eastern Central Anatolia, Turkey. Geol J 40:457–476

Özer E (1994) Stratigraphy of the Munzur mountains (Kemah-İliç-Erzincan). Bull Geol Soc Turk 37:53–64 (in Turkish with English abstract)

Özer E, Öner F (1999) Geochemical characteristics and tectonic interpretation of the Yakuplu Pluton in the northeastern Taurid Mountains, eastern Turkey. Chemie Erde 59:173–182 (in German with English abstract)

Özgenç İ, İlbeyli N (2009) Geochemical constraints on petrogenesis of Late Cretaceous alkaline magmatism in east-central Anatolia (Hasançelebi-Başören, Malatya), Turkey. Miner Petrol 95:71–85

Özgül N, Turşucu A, Özyardımcı N, Şenol M, Bingöl İ, Uysal S (1981) Munzur dağlarının jeolojisi. Min Res Explor Inst Turkey (MTA) Report 6995, Ankara (unpublished)

Parlak O (2006) Geodynamic significance of granitoid magmatism in the southeast Anatolian orogen: geochemical and geochronological evidence from Göksun-Afşin (Kahramanmaraş, Turkey) region. Int J Earth Sci 95:609–627

Pearce JA, Bender JF, De Long SE, Kidd WSF, Low PJ, Güner Y, Şaroğlu F, Yılmaz Y, Moorbath S, Mitchell JG (1990) Genesis of collision volcanism in Eastern Anatolia, Turkey. J Volcanol Geotherm Res 44:189–229

Pettke T, Oberli F, Heinrich CA (2010) The magma and metal source of giant porphyry-type ore deposits, based on lead isotope microanalysis of individual fluid inclusions. Earth Planet Sci Lett 296:267–277

Poisson A, Guezou JC, Öztürk A, İnan S, Temiz H, Gürsoy H, Kavak K, Özden S (1996) Tectonic setting and evolution of the Sivas Basin, Central Anatolia, Turkey. Int Geol Rev 38:838–853

Rice SP, Robertson AHF, Ustaömer T (2006) Late Cretaceous–Early Cenozoic tectonic evolution of the Eurasian active margin in the Central and Eastern Pontides, northern Turkey. In: Robertson AHF, Mountrakis D (eds) Tectonic development of the Eastern Mediterranean Region. Geol Soc Lond Spec Publ 260:413–445

Richards JP (2003a) Tectono-magmatic precursors for porphyry Cu–(Mo–Au) deposit formation. Econ Geol 96:1515–1533

Richards JP (2003b) Metallogeny of the Neo-Tethys arc in central Iran. In: Eliopoulos DG et al (eds) Proceedings of mineral exploration and sustainable development. Millpress, Rotterdam, pp 1237–1239

Richards JP (2009) Postsubduction porphyry Cu–Au and epithermal deposits: products of remelting of subduction-modified lithosphere. Geology 37:247–250

Richards JP (2011) Magmatic to hydrothermal metal fluxes in convergent and collided margins. Ore Geol Rev 40:1–26

Richards JP, Noble SR (1998) Application of radiogenic isotope systems to the timing and origin of hydrothermal processes. In: Richards JP, Larson PB (eds) Techniques in hydrothermal ore deposits geology: Soc Econ Geol, Reviews in Economic Geology 10:195–233

Rızaoğlu T, Parlak O, Höck V, Koller F, Hames WE, Billor Z (2009) Andean-type active margin formation in the eastern Taurides: geochemical and geochronological evidence from the Baskil granitoid (Elazığ, SE Turkey). Tectonophysics 473:188–207

Robertson AHF, Dixon JE (1984) Introduction: aspects of the geological evolution of the Eastern Mediterranean. In: Dixon JE,

Robertson AHF (eds) The geological evolution of the Eastern Mediterranean: Geol Soc Lond Spec Publ 17:1–74.

Robertson AHF, Pickett EA (2000) Palaeozoic-Early Tertiary Tethyan evolution of mélanges, rift and passive margin units in the Karaburun Peninsula (western Turkey) and Chios Island (Greece). In: Bozkurt E, Winchester, JA, Piper JDA (eds) Tectonics and magmatism in Turkey and surrounding area. Geol Soc Lond Spec Publ 173:43–82

Robertson AHF, Parlak O, Rızaoğlu T, Ünlügenç Ü, İnan N, Taşlı K, Ustaömer T (2007) Tectonic evolution of the South Tethyan ocean: evidence from the Eastern Taurus Mountains (Elazığ region, SE Turkey). In: Ries AC, Butler RWH, Graham RH (eds) Deformation of the continental crust: the legacy of Mike Coward. Geol Soc Lond Spec Publ 272:231–270

Román-Berdiel T, Gapais D, Brun JP (1997) Granite intrusion along strike-slip zones in experiment and nature. Am J Sci 297:651–678

Ryskamp EB, Abbott JT, Christiansen EH, Keith JD, Vervoort JD, Tingey DG (2008) Age and petrogenesis of volcanic and intrusive rocks in the Sulphur Spring Range, central Nevada: comparisons with ore-associated Eocene magma systems in the Great Basin. Geosphere 4:496–519

Sasso AM, Clark, AH (1998) The Farallòn Negro Group, northwest Argentina: magmatic, hydrothermal, and tectonic evolution and implications for Cu–Au metallogeny in the Andean back-arc. SEG Newsletter 34:1 and 8–18.

Schellart WP, Lister GS (2004) Tectonic models for the formation of arc-shaped convergent zones and backarc basins. In: Sussman AJ, Weil AB (eds) Orogenic curvature: integrating paleomagnetic and structural analyses. Geol Soc Am Spec Pap 383:237–258

Selby D, Creaser RA (2004) Macroscale NTIMS and microscale LA-MC-ICP-MS Re–Os isotopic analysis of molybdenite: testing spatial restrictions for reliable Re–Os age determinations, and implications for the decoupling of Re and Os within molybdenite. Geochim Cosmochim Acta 68:3897–3908

Şengör AMC, Yılmaz Y (1981) Tethyan evolution of Turkey: a plate tectonic approach. Tectonophysics 75:181–241

Şengör AMC, Özeren MS, Genç T, Zor E (2003) East Anatolian high plateau as a mantle-supported, north-south shortened domal structure. Geophys Res Lett 30:8045. doi:10.1029/2003GL017858

Shirey SB, Walker RJ (1995) Carius tube digestion for low-blank rhenium–osmium analysis. Anal Chem 67:2136–2141

Sillitoe RH (2008) Major gold deposits and belts of the North and South American Cordillera: distribution, tectonomagmatic settings, and metallogenic considerations. Econ Geol 103:663–687

Smoliar MI, Walker RJ, Morgan JW (1996) Re–Os ages of Group IIA, IIIA, IVA, and IVB iron meteorites. Science 271:1099–1102

Solomon M (1990) Subduction, arc reversal, and the origin of porphyry copper–gold deposits in island arcs. Geology 18:630–633

Stampfli GM (2000) Tethyan oceans. In: Bozkurt E, Winchester JA, Piper JDA (eds) Tectonics and magmatism in Turkey and surrounding area. Geol Soc Lond Spec Publ 173:1–23

Stampfli GM, Marcoux J, Baud A (1991) Tethyan margins in space and time. Palaeogeogr Palaeoclimatol Palaeoecol 87:373–410

Stolz AJ, Jochum KP, Spettel B, Hofmann AW (1996) Fluid- and melt-related enrichment in the subarc mantle: evidence from Nb/Ta variations in island-arc basalts. Geology 24:587–590

Sun S-S, McDonough WF (1989) Chemical and isotopic systematics of oceanic basalts: Implications for mantle composition and processes. In: Saunders AD, Norry MJ (eds) Magmatism in the ocean basins. Geol Soc Lond Spec Publ 42:313–345

Tekin UK, Göncüoğlu MC, Turhan N (2002) First evidence of Late Carnian radiolarians from the İzmir–Ankara suture complex, central Sakarya, Turkey: implications for the opening age of the İzmir-Ankara branch of Neo-Tethys. Geobios 35:127–135

Temiz H, Guezou JC, Poisson AM, Tutkun Z (1993) Tectonostratigraphy and kinematics of the eastern end of the Sivas Basin (central eastern Turkey): implications for the so-called 'Anatolian block'. Geol J 28:239–250

Topuz G, Altherr R, Schwarz WH, Siebel W, Satır M, Dokuz A (2005) Post-collisional plutonism with adakite-like signatures: the Eocene Saraycık granodiorite (Eastern Pontides, Turkey). Contrib Mineral Petrol 150:441–455

Tosdal RM, Richards JP (2001) Magmatic and structural controls on the development of porphyry Cu ± Mo ± Au deposits. In: Richards JP, Tosdal RM (eds) Structural controls on ore genesis. Rev Econ Geol 14:157–181

Tunç M, Özçelik O, Tutkun Z, Gökçe A (1991) Basic geological characteristics of the Divriği–Yakuplu–İliç–Hamo (Sivas) area. Turk J Eng Environ Sci 15:225–245 (in Turkish with English abstract)

Özgül N, Turşucu A (1984) Stratigraphy of the Mesozoic carbonate sequence of the Munzur Mountains (Eastern Turkey). In: Tekeli O, Göncüoğlu MC (eds) Geology of the Taurus Belt. Proceedings of the International Tauride Symposium. Mineral Research and Exploration Institute of Turkey (MTA) Publications, Ankara, Turkey, pp 173–180

Tüysüz O, Tekin UK (2007) Timing of imbrication of an active continental margin facing the northern branch of Neotethys, Kargı Massif, northern Turkey. Cret Res 28:754–764

Umhoefer PJ, Whitney DL, Teyssier C, Fayon AK, Casale G, Heizler MT (2007) Yo-yo tectonics in a wrench zone, Central Anatolian fault zone, Turkey. In: Till AB, Roeske SM, Sample JC, Foster DA (eds) Exhumation associated with continental strike-slip fault systems. Geol Soc Am Spec Pap 434:35–57

Van Dongen M, Weinberg RF, Tomkins AG, Armstrong RA, Woodhead JD (2010) Recycling of Proterozoic crust in Pleistocene juvenile magma and rapid formation of the Ok Tedi porphyry Cu–Au deposit, Papua New Guinea. Lithos 114:282–292

Verdel C, Wernicke BP, Hassanzadeh J, Guest B (2011) A Paleogene extensional arc flare-up in Iran. Tectonics 30:TC3008. doi: 10.1029/2010TC002809.

Vincent SJ, Allen MB, Ismail-Zadeh AD, Flecker R, Foland KA, Simmons MD (2005) Insights from the Talysh of Azerbaijan into the Paleogene evolution of the South Caspian region. Geol Soc Am Bull 117:1513–1533

Völkening J, Walczyk T, Heumann K (1991) Osmium isotope ratio determinations by negative ion mass spectrometry. Int J Mass Spectrom Ion Proc 105:147–159

Wallace LM, Ellis S, Mann P (2009) Collisional model for rapid fore-arc block rotations, arc curvature, and episodic back-arc rifting in subduction settings. Geochem Geophys Geosyst 10:Q01004. doi:10.1029/2008GC002220

Whitney DL, Umhoefer PJ, Teyssier C, Fayon AK (2008) Yo-yo tectonics of the Niğde Massif during wrenching in Central Anatolia. Turk J Earth Sci 17:209–217

Yalınız MK, Göncüoğlu MC, Özkan-Altıner S (2000) Formation and emplacement ages of the SSZ-type Neotethyan ophiolites in Central Anatolia. Turkey: palaeotectonic implications. Geol J 35:53–68

Yazgan E (1984) Geodynamic evolution of the Eastern Taurus region. In: Tekeli O, Göncüoğlu MC (eds) Geology of the Taurus Belt. Proceedings of the International Tauride Symposium. Mineral Research and Exploration Institute of Turkey (MTA) Publications, Ankara, Turkey, pp 199–208

Yazgan E, Chessex R (1991) Geology and tectonic evolution of Southeastern Taurus in the region of Malatya. Turk Assoc Petrol Geol Bull 3:1–42

Yiğit Ö (2009) Mineral deposits of Turkey in relation to Tethyan metallogeny: implications for future mineral exploration. Econ Geol 104:19–51

Yiğitbaş E, Yılmaz Y (1996a) New evidence and solution to the Maden complex controversy of the Southeast Anatolian orogenic belt (Turkey). Geol Rund 85:250–263

Yiğitbaş E, Yılmaz Y (1996b) Post-Late Cretaceous strike-slip tectonics and its implications for the Southeast Anatolian orogen, Turkey. Int Geol Rev 38:818–831

Yılmaz A (1985) Basic geological characteristics and structural evolution of the region between the Upper Kelkit Creek and the Munzur Mountains. Bull Geol Soc Turk 28:78–92 (in Turkish with English abstract)

Yılmaz Y (1993) New evidence and model on the evolution of Southeast Anatolian orogen. Geol Soc Am Bull 105:251–271

Yılmaz S, Boztuğ D, Öztürk A (1993) Geological setting, petrographic and geochemical characteristics of the Cretaceous and Tertiary igneous rocks in the Hekimhan-Hasançelebi area, north-west Malatya, Turkey. Geol J 28:383–398

Zeck HP, Ünlü T (1991) Shoshonitic, monzonitic pluton near Murmano, eastern central Turkey—a preliminary note. Bull Min Res Explor Inst Turkey (MTA) 112:47–58 (in Turkish with English abstract)